Accepted Manuscript

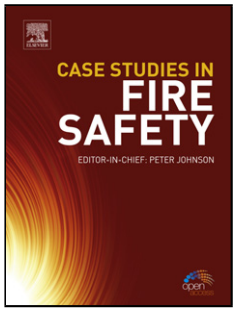

Title: Hydrogen trapping in some advanced high strength steels

Author: Qinglong Liu Jeffrey Venezuela Mingxing Zhang Qingjun Zhou Andrej Atrens

PII: S0010-938X(16)30268-2
DOI: http://dx.doi.org/doi:10.1016/j.corsci.2016.05.046
Reference: CS 6807

To appear in:

Received date: 7-10-2015
Revised date: 26-5-2016
Accepted date: 31-5-2016

Please cite this article as: Qinglong Liu, Jeffrey Venezuela, Mingxing Zhang, Qingjun Zhou, Andrej Atrens, Hydrogen trapping in some advanced high strength steels, Corrosion Science http://dx.doi.org/10.1016/j.corsci.2016.05.046

Hydrogen trapping in some advanced high strength steels

Qinglong Liu[1], Jeffrey Venezuela, Mingxing Zhang[1], Qingjun Zhou[2], Andrej Atrens[1,*]

[1] The University of Queensland, Division of Materials, School of Mining and Mechanical Engineering, St. Lucia, 4072 Australia

[*] Corresponding author, andrejs.atrens@uq.edu.au, +61 7 3365 3748

[2] Baoshan Iron & Steel Co., Ltd, Research Institute, Shanghai, 201900, China

Highlights

Permeability experiments were used to study hydrogen diffusion and trapping

The trapping effect was less significant at a more negative charging potential

The lattice diffusion coefficient of hydrogen was measured

The densities of reversible hydrogen trap sites was ~ 2×10^{18} sites cm^{-2}

Abstract

Permeability experiments were used to study hydrogen diffusion and trapping in dual phase (DP), and quenched and portioned (Q&P), advanced high strength steels. The measured reversible hydrogen trap densities indicated that (i) trapping was less significant at a more negative potential, and (ii) the lattice diffusion coefficient of hydrogen could be measured from the partial transients at the most negative potentials. The densities of reversible hydrogen traps evaluated from complete decays from -1.700 $V_{Hg/HgO}$ were ~ 2×10^{18} sites cm^{-2}, and were a factor of two higher than those from partial decay transients between -1.700 $V_{Hg/HgO}$ and -1.100 $V_{Hg/HgO}$.

Keywords: A. Steel, B. Hydrogen permeation, C. Potentiostatic

1. Introduction

1.1 Advanced high strength steels (AHSS)

Advanced high strength steels (AHSS) were developed, and have been adopted, for auto components to reduce vehicle weight and to increase vehicle safety [1-4]. This paper characterises hydrogen trapping in some AHSS and thereby adds to the knowledge base regarding AHSS.

The AHSS include Dual Phase (DP) steels, Complex-Phase (CP) steels, Ferritic-Bainitic (FB) steels, Martensitic (MS) steels, Transformation-Induced Plasticity (TRIP) steels, Hot-Formed (HF) steels, and Twinning-Induced Plasticity (TWIP) steels [3].

DP steels have a microstructure of ferrite and martensite. The soft, continuous, ferrite matrix produces good formability. The hard martensitic phase is dispersed in the ferrite matrix and contributes to the high strength, and high strain hardening. As a result, vehicle components made from DP steels have a high capacity to absorb energy [5]. DP steel components may be galvanised for corrosion protection in service.

Transformation induced plasticity (TRIP) steels have a microstructure of a ferrite matrix, islands of retained austenite, and dispersed bainite. Martensite is also commonly present. Transformation of retained austenite to martensite causes the transformation induced plasticity, and also causes an increased strain hardening rate at higher strain levels [6]. TRIP steel components also have a good ability to absorb energy [5].

Quenching and partitioning (Q&P) is a new heat treatment to produce TRIP steel. The microstructure [7] contains more retained austenite at room temperature [8, 9], resulting in a greater TRIP effect. As a result, their ductility, formability and strain-hardening rate are greater than other steels with comparable strength. Q&P steels are thus third generation AHSS with high strength and high-ductility [10].

1.2 Hydrogen sources in service

Hydrogen embrittlement (HE) can occur in AHSS [11, 12]. The hydrogen can be liberated by corrosion of the steel of the car body in service. In neutral and alkaline solutions, the hydrogen evolution occurs by the following cathodic partial reaction [13]:

$$H_2O + M + e \rightarrow MH_{ads} + OH^- \quad (1)$$

where M represents the metal surface and MH_{ads} represents hydrogen adsorbed on the metal surface. The atomic hydrogen may be desorbed by the desorption reaction given by Eq. (2), through which two adsorbed hydrogen atoms combine to a molecule of hydrogen that leaves the metal surface, or by the electrochemical desorption reaction given by Eq. (3).

$$2MH_{ads} \leftrightarrow H_2 + 2M \quad (2)$$

$$MH_{ads} + H_2O + e \rightarrow H_2 + OH^- + M \quad (3)$$

Some of the adsorbed hydrogen enters the metal, MH_{abs}, by the following equilibrium reaction:

$$MH_{ads} \leftrightarrow MH_{abs} \quad (4)$$

The hydrogen in the steel, in combination with an applied stress, can cause hydrogen embrittlement (HE), which is of particular concern for high-strength steels [14], such as the AHSS.

1.3 Hydrogen trapping

Hydrogen diffusion is often studied using the permeation technique of Devanathan and Stachurski [15]. This permeation method can provide quantitative information, such as the effective hydrogen diffusion coefficient, D_{eff}, the hydrogen concentration, C_H, and the

hydrogen trapping site density. This permeation technique was used in the present research to study hydrogen diffusion and trapping in DP and Q&P AHSS.

Hydrogen atoms are located in interstitial sites and are trapped by microstructure features such as voids, dislocations, grain boundaries, carbide interfaces, and impurities [16-18]. These hydrogen traps play an important role in the transportation and distribution of hydrogen in the steel [18]. Hydrogen traps are characterized as irreversible traps and reversible traps [19-21]. Irreversible traps are sites with a high trap activation energy, and thus the trapped hydrogen is considered as non-diffusible. Examples of irreversible traps are carbide interfaces, incoherent precipitates, and high-angle grain boundaries. In contrast, hydrogen de-trapping is easier from trap sites with lower activation energy. These sites are characterized as reversible traps. Examples are dislocations, low-angle grain boundaries, coherent precipitates and twin boundaries. Hydrogen trapped in reversible hydrogen trap sites is diffusible. These reversible hydrogen traps influence hydrogen diffusion and have an influence on the hydrogen embrittlement of the steel [22].

Hydrogen trapping can be characterised by the parameters: the hydrogen-trap binding energy, E_b, and the density of trap sites, N_t. Hydrogen trapping was incorporated into a kinetic diffusion model by McNabb and Foster [23]. This model was reformulated by Oriani [24] using the assumption that there is a local equilibrium between trapped hydrogen atoms and mobile hydrogen. Based on the Oriani [24] model, Dong et al. [25] proposed that the number of hydrogen-trap sites per unit volume, N_t, could be evaluated from:

$$\ln\left(\frac{D_L}{D_{eff}} - 1\right) = \ln\frac{N_t}{N_L} + \frac{E_b}{RT} \quad (5)$$

where, D_L is the lattice diffusion coefficient for hydrogen, D_{eff} is the effective diffusion coefficient for hydrogen in the presence of traps, N_L is the density of the interstitial sites in the steel, E_b is the hydrogen-trap binding energy, R is the gas constant, and T is the absolute temperature. This model is designated as the Oriani-Dong model in this paper.

Hydrogen trapping can be minimized by successive partial permeation rise transients after which the following permeation rise transients are controlled by lattice diffusion, because all the hydrogen traps are full [26, 27].

Permeation decay transients, in contrast, are sensitive to the de-trapping of hydrogen, and can be used to evaluate the amount of reversibly trapped hydrogen [27-29], as illustrated in Fig. 1, adapted from Liu and Atrens [29]. The area under the experimental desorption permeation curve corresponds to the total amount of diffusible and trapped hydrogen. The area under the corresponding theoretical permeation decay curve, evaluated using the lattice

diffusion coefficient, D_L, corresponds to the amount of diffusible hydrogen. By subtraction, the area difference between the two curves, as illustrated by the shaded part in Fig. 1, represents the amount of reversible trapped hydrogen. This method is called the permeation curve method herein.

The permeation curve method indicates that the density of reversible hydrogen traps, designated as N_t^*, is given by [27, 29]:

$$N_t^* = \frac{12.5 \times 10^{18}\, s}{L} \tag{6}$$

where s is the difference in area between the experimental decay curve and the theoretical decay curve evaluated using the lattice diffusion coefficient, D_L, and L is the thickness of the specimen. Eq. (6) assumes that there is only one type of reversible trap for hydrogen, and that each trap holds one hydrogen atom.

The concentration of the trapped hydrogen is given by [29]:

$$C_T^* = \frac{N_t^*}{N_A} \tag{7}$$

where N_A is the Avogadro constant with value of 6.02×10^{23} mol^{-1}.

This permeation curve method was applied by Zakroczymski [27] to Armco iron. Complete decay transients, where complete discharge was allowed, indicated that the reversibly trapped hydrogen corresponded to 98% of the total amount of absorbed hydrogen. This method was also used to measure the density of reversible hydrogen traps influencing hydrogen diffusion between cathodic charging potentials of $-1.700\ V_{Ag/AgCl}$ and $-1.100\ V_{Ag/AgCl}$ for a 3.5NiCrMoV medium strength steel [29]. The density of reversible traps was $\sim 10^{18}$ sites cm^{-3}. In this case the total amount of trapped hydrogen was not measured.

These techniques have not been applied to advanced high strength steels (AHSS) to measure the density of hydrogen traps.

1.4 Scope of current research

The current work (i) studies hydrogen diffusion in DP and Q&P grades of AHSS using permeability experiments, (ii) evaluates the density of reversible hydrogen traps that influence the hydrogen diffusion under these charging conditions using (a) the Oriani-Dong model and (b) the permeation curve method, and (iii) evaluates the total density of reversible hydrogen trap sites from complete permeation decay curves.

2. Experimental Methods

2.1 Materials

The DP and Q&P steels were commercial steels, supplied as rolled sheets, and were designated as follows: 980 DP, 980 DP-GI (650 MPa YS), 980 DP-GI (700 MPa YS), 1200 DP-GI, and 980 QP. The average sheet thicknesses were 1.35 mm for 980 DP and 1200 DP-GI, 0.95mm for 980 DP-GI (650 MPa YS), 0.99 mm for 980 DP-GI (700 MPa YS), and 1.93 mm for 980 QP. Table 1 presents the chemical composition and mechanical properties as provided by the steel supplier.

The microstructures of the DP and Q&P steels were examined using a light microscope (LM), and using a scanning electron microscope (SEM), after metallographic polishing to 1 μm and etching with a nital solution. The volume fraction of each phase was evaluated using the point counting method, as described in ASTM E562 [30]. The grain size were estimated by the linear intercept method [31, 32] for DP steels, and using the microscope calibration bar for Q&P steels.

2.2 Permeability experiments

Fig. 2 presents the double cell, permeability apparatus, which was based on that of Devanathan and Stachurski [27], and was similar to that of Liu and Atrens [29]. The two cells were separated by the test specimen in the form of a flat sheet, which was the working electrode for each cell. Each cell also contained a 0.1 M NaOH solution, a Pt wire as the counter electrode, and a Luggin capillary connected to an Hg/HgO, KOH (20%) reference electrode, the potential of which is +0.098 V_{SHE}. Experiments were carried out at room temperature of 23 ± 2 ℃.

The specimen side exposed to left-hand-side cell was polished to 3 μm. The left-hand-side cell was the hydrogen entry side. Hydrogen was liberated on the left-hand-side surface of the specimen by a negative potential applied using a MP 81 potentiostat.

The right-hand side was the hydrogen exit side. The 0.1 M NaOH solution was deaerated on this side to ensure a low background current density. N_2 was bubbled throughout the whole experiment to remove oxygen, which would contribute to the oxidation current density. The exit side background current density was lower than 0.2 μA cm^{-2} before cathodic charging commenced on the hydrogen entry side. On the right hand side, a

PARSTAT 2273 potentiostat maintained a potential of +300 $mV_{Hg/HgO}$ to oxidise the emerging hydrogen, and the corresponding current measured the amount of permeated hydrogen.

The hydrogen exit side of the specimen was plated with palladium to prevent oxidation of the steel. The processes for palladium (Pd) plating was as follows: the specimen was ground to 1200 grit SiC paper on the side to be Pd coated; cleaned for 15 min at 80 ℃ in an oil-removal aqueous solution, containing NaOH 16 g L^{-1}, Na_2CO_3 15 g L^{-1}, $Na_3PO_4 \cdot 12H_2O$ 15 g L^{-1} and detergent 2 ml L^{-1}; washed with distilled water, dried with flowing air, and weighed. The non-palladium-plating side was masked with an adhesive sticker and a conductive wire was attached to the edge of the specimen. The specimen was pickled in 32% HCl solution for 5 s and thoroughly washed with distilled water; electroplated in a solution consisting of 5 g $PdCl_2$ in 1 L of 25 wt% ammonia, at a current density of 2-3 mA cm^{-2} for 5 min with stirring during the whole plating time; rinsed immediately with ethanol, dried with flowing air and weighed. The increase in weight was used to calculate the thickness of the Pd coating, which was typically about 0.5 μm.

A long-time uninterrupted cathodic pre-charging was found by Zakroczymski [27, 33, 34] to stabilize the metal surface and minimized the surface effect. A similarly long-time pre-charging was used in this study. Pre-charging, at –1.600 $V_{Hg/HgO}$, was (i) for 48 hour for 980 DP-GI (650 MPa YS) and 980 DP-GI (700 MPa YS), and (ii) for 60 hour for 980 DP, 1200 DP-GI and 980 QP.

After the cathodic pre-charging, successive transients were measured, such as those from – 1.600 $V_{Hg/HgO}$ to – 1.700 $V_{Hg/HgO}$, as well as a transient loop from – 1.700 $V_{Hg/HgO}$ to – 1.100 $V_{Hg/HgO}$ and back to – 1.700 $V_{Hg/HgO}$. The potentials for the transient loop were: – 1.700 $V_{Hg/HgO}$, – 1.600 $V_{Hg/HgO}$, – 1.400 $V_{Hg/HgO}$, – 1.200 $V_{Hg/HgO}$, – 1.100 $V_{Hg/HgO}$, and similarly back to – 1.700 $V_{Hg/HgO}$.

After the permeation current density achieved steady state at – 1.700 $V_{Hg/HgO}$, the charging potential at the entry side was set to the open circuit potential (ocp) so that there was no hydrogen produced on the entry side, and a complete decay transient was measured.

The same experimental sequence was carried out for each steel.

The permeation transients have the following form [27, 35]:

$$i_n = \frac{i_p - i_p^0}{i_p^\infty - i_p^0} = \frac{2L}{\sqrt{\pi D t}} \sum_{n=0}^{\infty} \exp\left(- \frac{(2n+1)^2 L^2}{4Dt} \right) \qquad \text{(Rise transients)} \qquad (8)$$

$$i_n = \frac{i_p - i_p^\infty}{i_p^0 - i_p^\infty} = 1 - \frac{2L}{\sqrt{\pi D t}} \sum_{n=0}^{\infty} \exp\left(-\frac{(2n+1)^2 L^2}{4Dt}\right) \quad \text{(Decay transients)} \quad (9)$$

where i_n is the normalized current, which increases from 0 to 1 for a rise transient, i_p is the measured permeation current density at time t, i_p^0 is the initial steady-state permeation rate at time $t = 0$, i_p^∞ is the new steady-state permeation current density, and L is the thickness of the steel sheet. For the first charging, $i_p^0 = 0$, and for the complete decay $i_p^\infty = 0$. The experimental permeation curves were fitted to Eq. (8) or (9), to determine the diffusion coefficient, D. During the first few transients, there were empty traps, which would retard hydrogen diffusion, so that the fitted D values were considered as the effective diffusion coefficient, D_{eff}. For subsequent transients, most of the traps were filled, and the evaluated D values were similar to each other and were close to the lattice value, especially for transients at more negative potentials with less trapping effect, and the lattice diffusion coefficient, D_L, could be determined [26, 29].

The lattice hydrogen concentration, C_L, at the sub-surface on the cathodic side, was calculated from:

$$C_L = \frac{i_p^\infty L}{F D_L} \quad (10)$$

and the total hydrogen concentration, C_T, was evaluated from

$$C_T = \frac{i_p^\infty L}{F D_{eff}} \quad (11)$$

where F is the Faraday constant, L is the thickness of the membrane, i_p^∞ is the steady-state permeation rate, D_L is the lattice diffusion coefficient of hydrogen in the specimen material, and D_{eff} is the measured effective diffusion coefficient of hydrogen in the specimen material. The hydrogen concentration, C, was expressed in units of mol m^{-3}, and was also converted to μg g^{-1}, which represented the weight of hydrogen per gram of the steel.

The density of reversible traps was evaluated using (i) the Oriani-Dong model and (ii) the permeation curve method, as outlined in the Introduction.

3. Results

3.1 Microstructure

Fig. 3(a) presents a SEM image of the typical DP steel microstructure, which consisted of the ferrite matrix, marked 'F', and martensite islands (M) embedded along ferrite grain boundaries. The martensite, as revealed by the nital etchant, consisted of a needle-like structure and appeared embossed. The ferrite appeared dark and smooth, and not as embossed as the martensite. Table 2 presents the relative amounts and grain sizes of the constituent phases in each steel. There was a decreasing amount of ferrite and an increasing amount of martensite for the DP steels in the following order 980 DP, 980 DP-GI (650 MPa YS), 980 DP-GI (700 MPa YS) and 1200DP-GI. This correlated with the increasing yield strength. The ferrite and martensite grain sizes were comparable.

Fig. 3(b) presents a typical microstructure of the 980 QP steel viewed with a light microscope. The microstructure consisted of ferrite, bainite and retained austenite. The ferrite appeared yellow. The bainite appeared brown. The retained austenite appeared as the small white blocks dispersed in the ferrite and the bainite. Table 2 indicates that the volume fraction of ferrite, bainite and retained austenite was 39%, 53% and 8%, respectively. The grain sizes of ferrite and martensite were similar and were significantly larger than that of the retained austenite.

3.2 Cathodic pre-charging

Fig. 4 presents the hydrogen permeation current density versus time for the four DP steels and the Q&P steel during long-time pre-charging in the 0.1 M NaOH solution at -1.600 $V_{Hg/HgO}$, which was started after the background current density in the right hand cell decreased to less than 0.2 μA cm^{-2}. The breakthrough time was about 315 s, 1235 s, 1503 s, 1184 s and 810 s for 980 DP, 980 DP-GI (650 MPa YS), 980 DP-GI (700 MPa YS), 1200 DP-GI, and 980 QP, respectively. Thereafter, the current density increased significantly, reached a maximum for 980 DP-GI (650 MPa YS) and 980 DP-GI (700 MPa YS) and decreased somewhat for these steels. The significant increase in permeation current density with cathodic pre-charging time was consistent with the literature [33, 34], and is attributed to a stabilisation of the steel surface due to (i) the reduction of some of the air-formed oxide, which increased the surface coverage of hydrogen, and (ii) the weakening of the bonding force between the adsorbed hydrogen and the steel, which facilitated hydrogen absorption by reaction (4). The subsequent decrease of the permeation current density at longer charging

times is attributed to the formation of surface products such as iron oxy-hydroxide, which provide some hindrance of the entry of adsorbed hydrogen into the steel.

The maximum current density indicated approximately steady-state hydrogen charging conditions. These conditions were reached for 980 DP-GI (650 MPa YS) and 980 DP-GI (700 MPa YS) in about 33 hour, at which time the steady-state current density was 23 μA cm^{-2} and 13 μA cm^{-2}, respectively. For 980 DP, 1200 DP-GI and 980 QP steels, reaching steady state required about 60 hour, at which time the steady-state current density was 32 μA cm^{-2}, 21 μA cm^{-2} and 7 μA cm^{-2}, respectively.

Pre-charging was carried out for the subsequent experiments for 48 hour for the 980 DP-GI (650 MPa YS) and 980 DP-GI (700 MPa YS) steels, and 60 hour for the other steels, so that there would be a similar surface state.

3.3 Permeation Transients

Fig. 5(a) presents two typical subsequent partial rise transients. These were identical, indicating that the long-time pre-charging had filled the reversible traps. Fig. 5(b) shows corresponding decay transients. The second decay transient was slower, indicating that it took longer time for the hydrogen to permeate through the steel sheet specimen to reach steady state, due to the retardation of hydrogen diffusion by trapping.

Table 3 presents values of the diffusion coefficient, evaluated by fitting Eq. (8) and (9) by Matlab to each experimental permeation transient, obtained from successive transients and from the transient loop. The values of diffusion coefficient were similar for the first two rise transients from -1.600 $V_{Hg/HgO}$ and – 1.700 $V_{Hg/HgO}$ after long time pre-charging, and these values of the diffusion coefficient are identified as the lattice diffusion coefficient, D_L. The diffusion coefficients measured for the subsequent decay transients gave decreasing values of D_{eff}. Thereafter the partial rise transients gave values of the effective diffusion coefficient, D_{eff}, that increased towards the value for the lattice diffusion coefficient.

Fig. 6 presents the fitting of rise and decay transients to the theoretical curves for 980 DP-GI (650 MPa YS) steel. Fig. 6(a) shows the normalized experimental rise transient from – 1.600 $V_{Hg/HgO}$ and – 1.700 $V_{Hg/HgO}$, which was well fitted by the theoretical curve. This indicated that when the cathodic potential decreased to the more negative value, the hydrogen concentration at the subsurface immediately changed to the new constant value, the hydrogen diffusion was controlled by lattice diffusion, and that trapping was negligible. The fitted value of 1.58×10^{-6} cm^2 s^{-1} was identified as the hydrogen lattice diffusion coefficient, D_L,

for 980 DP-GI (650 MPa YS) steel. In contrast, for the decay transients, as shown in Fig. 6(b), the fitting was not as good as those for rise transients, attributed to the influence of trapping.

There was the same trend for each steel. This allowed determination of the hydrogen lattice diffusion coefficient, D_L, for each steel: 2.07×10^{-6} cm^2 s^{-1}, 0.76×10^{-6} cm^2 s^{-1}, 1.27×10^{-6} cm^2 s^{-1} and 0.68×10^{-6} cm^2 s^{-1} for 980 DP, 980 DP-GI (700 MPa YS), 1200 DP-GI and 980 QP steels, respectively.

Fig. 7 presents a transient loop from -1.700 $V_{Hg/HgO}$ to -1.100 $V_{Hg/HgO}$ and back to -1.700 $V_{Hg/HgO}$ in the 0.1 M NaOH solution for 980 DP-GI (650 MPa YS) steel. Each transient was a partial transient, which meant that there was always a significant charging potential applied to the specimen, and the specimen was not allowed to completely discharge all hydrogen. Similar transient loops were also carried out for other DP and Q&P steel grades. Each experimental transient was fitted by Matlab to Eq. (8) or Eq. (9) to determine the hydrogen diffusion coefficient values.

Table 3 presents the values of hydrogen diffusion coefficient, the steady-state current density and the hydrogen concentration, evaluated using Eq.(10). Fig. 7 and Table 3 indicate that as the charging potential was changed from -1.700 $V_{Hg/HgO}$ to -1.100 $V_{Hg/HgO}$ the steady-state current density and the hydrogen concentration at each potential decreased, indicating less hydrogen entered and permeated through the steel at a less negative charging potential. When the charging potential was increased from -1.100 $V_{Hg/HgO}$ to -1.700 $V_{Hg/HgO}$, there was more hydrogen entering and permeating through the specimen, providing a higher steady-state current density and hydrogen concentration. Venezuela et al. [36] stated that during cathodic charging in the 0.1M NaOH solution, an increasingly negative charging potential lead to an increased hydrogen fugacity, as also found by Liu et al. [33], and thus an increased hydrogen concentration in the steel. They further found that this increased hydrogen concentration increased the susceptibility of martensitic advanced high strength steels to hydrogen embrittlement. The steady-state current density at -1.700 $V_{Hg/HgO}$ at the end of the loop was somewhat lower than that at -1.700 $V_{Hg/HgO}$ at the beginning of the loop, attributed to a slight change of the surface during the transients. This is consistent with the decrease of the permeation current density after peaking, as shown in Fig. 4.

4.0 Trap density evaluations

4.1 Oriani-Dong model

Table 4 presents the values of the density of reversible hydrogen trap sites, N_t, evaluated from the successive partial decay transients from the transient loop, evaluated using the Oriani-Dong model using Eq. (5) with (i) the hydrogen lattice diffusion coefficient as presented in part 3.3, (ii) N_L = 7.2 × 10^{22} cm^{-3} [25], (iii) E_b = 28.9 kJ mol^{-1} [16], and (iv) values of D_{eff} as listed in Table 3 for each transient. This particular value of binding energy was chosen because it is in the middle of the range of binding energies for reversible traps, and was the value used in our prior study [29].

Table 4 indicates that the trap density increased as the charging potential became less negative. For example, for 980 DP-GI (650 MPa YS), for the decay transient from the most negative charging condition from -1.700 $V_{Hg/HgO}$ to -1.600 $V_{Hg/HgO}$, the N_t value of 0.39 × 10^{17} sites cm^{-3} was the smallest. In contrast, the N_t value of 6.82 × 10^{17} sites cm^{-3} was the largest for decay transient that involved the least negative charging conditions (i.e. from -1.200 $V_{Hg/HgO}$ to -1.100 $V_{Hg/HgO}$). Similarly, for 980 QP, the minimum N_t value of 0.81 × 10^{17} sites cm^{-3} was evaluated for the transient from -1.700 $V_{Hg/HgO}$ to -1.600 $V_{Hg/HgO}$, whereas the maximum value of 5.40 × 10^{17} sites cm^{-3} was evaluated for the decay transient from -1.200 $V_{Hg/HgO}$ to -1.100 $V_{Hg/HgO}$. There was the same trend for each steel.

The hydrogen trap site density decreased with more negative charging during decay transients. This was attributed to the fact that the reversible traps in each steel were emptied step by step during successive each decay transient. At a less negative potential, more of the filled traps were emptied, leading to more interactions between the traps and diffused hydrogen, and thus there was a higher value for the trap site density. The trend that the hydrogen trap site density decreased with more negative charging potentials, resulting in a less potent trapping effect, was also consistent with the results that the hydrogen diffusion coefficient, D_{eff}, increased with more negative charging potential.

The density of the emptied reversible trap sites provided the amount of reversible trapped hydrogen for a particular condition, if it is assumed that there was only one hydrogen atom trapped at each reversible trap. For example, for 980 DP-GI (650 MPa YS) steel, when the charging potential was decreased from -1.700 $V_{Hg/HgO}$ to -1.600 $V_{Hg/HgO}$, the N_t value was 0.39 × 10^{17} sites cm^{-3}, indicating that 0.39 × 10^{17} sites cm^{-3} were emptied under this charging condition, and the trapped hydrogen concentration C_t was ~ 0.06 mol m^{-3} at -1.700 $V_{Hg/HgO}$. For comparison, the lattice hydrogen concentration, C_L, was calculated from Eq. (10), which at -1.700 $V_{Hg/HgO}$ was calculated to be 13.3 mol m^{-3}. Thus, the reversibly trapped hydrogen accounted for 0.5 % of the total absorbed hydrogen, which was the sum of trapped and lattice hydrogen.

Using this approach, for 980 DP-GI (650 MPa YS) steel, the amount of reversibly trapped hydrogen was equal to 3 %, 13 % and 37 % of the total absorbed hydrogen for the decay transient from -1.600 $V_{Hg/HgO}$ to -1.400 $V_{Hg/HgO}$, from -1.400 $V_{Hg/HgO}$ to -1.200 $V_{Hg/HgO}$, and from -1.200 $V_{Hg/HgO}$ to -1.100 $V_{Hg/HgO}$, respectively. The increasing portion of trapped hydrogen was consistent with the fact that the hydrogen trapping effect was more significant at a less negative charging potential.

Similarly, the percentage of trapped hydrogen at each charging potential from -1.700 $V_{Hg/HgO}$ to -1.600 $V_{Hg/HgO}$, from -1.600 $V_{Hg/HgO}$ to -1.400 $V_{Hg/HgO}$, from -1.400 $V_{Hg/HgO}$ to -1.200 $V_{Hg/HgO}$, and from -1.200 $V_{Hg/HgO}$ to -1.100 $V_{Hg/HgO}$, was 1 %, 3 %, 15 % and 45 %, respectively, for 980 DP steel, and the corresponding percentage at each charging potential was 1 %, 3 %, 9 % and 21 % for 980 DP-GI (700 MPa YS) steel, 0.3 %, 1 %, 6 % and 19 % for 1200DP-GI steel and 2 %, 7 %, 18 % and 42 % for 980 QP steel.

It is assumed that the reversible hydrogen traps were emptied step by step during the partial transients. The total density of the emptied traps could be considered as the sum of traps evaluated from each transient. Thus, the density of hydrogen trap sites for the decay transients from -1.700 $V_{Hg/HgO}$ to -1.100 $V_{Hg/HgO}$ was 12.8×10^{17} sites cm^{-3} for 980 DP, 14.4×10^{17} sites cm^{-3} for 980 DP-GI (650 MPa YS), 8.42×10^{17} sites cm^{-3} for 980 DP-GI (700 MPa YS), 7.04×10^{17} sites cm^{-3} for 1200 DP-GI and 12.4×10^{17} sites cm^{-3} for 980 QP steel.

Table 4 also includes values of the total hydrogen concentration, C_T, evaluated using Eq.(11). This value of total trapped hydrogen was in good agreement with the value of trapped hydrogen evaluated as the sum of trapped hydrogen concentration, C_t, and the lattice hydrogen concentration, C_L.

4.2 Permeation curves

Fig. 8(a) presents the decay transients obtained at various applied potentials and the theoretical curve calculated with a D_L value of 1.58×10^{-6} cm^2 s^{-1} for 980 DP-GI (650 MPa YS). Fig. 8(b) presents the corresponding normalised curves. The area difference, between each decay transient curve and the theoretical curve, is shown shaded in Fig. 8(a). This area increased with less negative applied potential and then decreased for the transient from -1.200 $V_{Hg/HgO}$ to -1.100 $V_{Hg/HgO}$. As stated above in the Introduction, the area difference between the experimental curve and the theoretical curve provided a measurement of the amount of trapped hydrogen. Thus, the general increased area difference indicated that there was more hydrogen trapped at a less negative potential, consistent with a more potent trapping effect at

a less negative potential. This same trend also occurred for each DP and Q&P steel, indicating that a more potent trapping effect at a less negative potential for each steel.

Table 4 presents the values for the density of reversibly trapped hydrogen, N_t^*, evaluated from the difference between the experimental permeation curve and the theoretical curve as illustrated in Fig. 8(a), and Eq. (6). Table 4 also presents the concentration of the trapped hydrogen, C_t^*, and the concentration of lattice hydrogen, C_L^*, which was evaluated based on the proportion of the shaded area to the area below the theoretical curve. Due to different values of i_0 and i_∞, the area below the theoretical curve was different for each partial decay transient, resulting in changed values of C_L^*. From -1.700 $V_{Hg/HgO}$ to -1.100 $V_{Hg/HgO}$ for the 980 DP-GI (650 MPa YS) steel, the trap site density, N_t^*, was 0.50×10^{17} sites cm^{-3}, 3.26×10^{17} sites cm^{-3}, 5.68×10^{17} sites cm^{-3}, 1.88×10^{17} sites cm^{-3} for each successive decay transient. The trap site density value, N_t^*, from -1.700 $V_{Hg/HgO}$ to -1.600 $V_{Hg/HgO}$ was comparable to that, N_t, obtained using Oriani-Dong model, for 980 DP-GI (650 MPa YS) and also for each steel. In general, the trap site density was higher at a less negative potential for each steels evaluated using this permeation curve method.

For the 980 DP-GI (650 MPa YS) steel, the concentration of trapped hydrogen for the decay transient from -1.400 $V_{Hg/HgO}$ to -1.200 $V_{Hg/HgO}$, as shown in Fig. 8(a), was calculated to be ~ 0.94 mol m^{-3}. Based on the area below the theoretical curve, the corresponding lattice hydrogen concentration at -1.400 $V_{Hg/HgO}$ was calculated to be ~ 5.50 mol m^{-3}. The trapped hydrogen corresponded to 15 % of the total amount of hydrogen from -1.400 $V_{Hg/HgO}$ to -1.200 $V_{Hg/HgO}$. Correspondingly, the reversibly trapped hydrogen from -1.700 $V_{Hg/HgO}$ to -1.600 $V_{Hg/HgO}$, from -1.600 $V_{Hg/HgO}$ to -1.400 $V_{Hg/HgO}$, from -1.400 $V_{Hg/HgO}$ to -1.200 $V_{Hg/HgO}$, and from -1.200 $V_{Hg/HgO}$ to -1.100 $V_{Hg/HgO}$, accounted for 0.6 %, 4 %, 15% and 18 % of the total absorbed hydrogen, respectively. The portion of trapped hydrogen also increased with less negative potential, consistent with the results from Oriani-Dong model.

Table 4 also presents the calculated N_t^*, C_t^* and C_L^* values for all the other steels. In all cases the percentage of trapped hydrogen increased from -1.700 $V_{Hg/HgO}$ to -1.100 $V_{Hg/HgO}$. The percentage of trapped hydrogen was 1 %, 5 %, 14 % and 17%, respectively for 980 DP steel; 1 %, 4 %, 6 % and 10 % for 980 DP-GI (700 MPa YS) steel; 0.3 %, 1 %, 7 % and 9 % for 1200 DP-GI steel, and 1 %, 2 %, 5 % and 7 % for 980 QP steel.

The total density of reversibly trapped hydrogen was the sum of the density from each transient. The total trap site density influencing the hydrogen diffusion between -1.700 $V_{Hg/HgO}$ to -1.100 $V_{Hg/HgO}$ was 10.1×10^{17} sites cm^{-3} for 980 DP, 11.1×10^{17} sites cm^{-3} for 980 DP-GI (650 MPa YS), 6.24×10^{17} sites cm^{-3} for 980 DP-GI (700 MPa YS), 5.08×10^{17} sites

cm^{-3} for 1200 DP-GI and 3.12×10^{17} sites cm^{-3} for 980 QP. The trap density values, N_t^*, for all the DP steels were between 20 ~ 30 % lower than those evaluated from Oriani-Dong model for the same steels. Similarly, the N_t^* value was 3.12×10^{17} sites cm^{-3} from the permeation curve method, about a quarter of the value obtained from Oriani-Dong model.

4.3 Complete decay transients

Fig. 9 presents the area difference between the experimental complete decay curve and the theoretical curve for 980 DP-GI (650 MPa YS) steel and 980 QP steel. The complete decay transient curve was obtained by discharging on the hydrogen entry side, meaning the charging potential was changed to the open circuit potential (ocp) from -1.700 $V_{Hg/HgO}$, so that there was no hydrogen being introduced into the specimen. According to the permeation curve method, the area of the shaded parts in Fig. 9(a) and (b) reflect the total amount of reversible hydrogen trap sites that were emptied from -1.700 $V_{Hg/HgO}$ to 0 V_{SHE}, and the area below the theoretical curve provided the amount of lattice diffused hydrogen at -1.700 $V_{Hg/HgO}$. This area difference between the experimental complete decay curve and the theoretical one was obtained for all the steels. Table 5 presents the values of the trap site density N_t^*, the trapped hydrogen concentration C_t^*, the concentration of lattice diffused hydrogen C_L^* and the percentage of trapped hydrogen.

Table 5 indicated that, for 980 DP-GI (650 MPa YS) steel, the trap site density N_t^* from -1.700 $V_{Hg/HgO}$ to 0 V_{SHE} was 2.42×10^{18} sites cm^{-3}. Assuming one hydrogen atom occupied one trap site, the corresponding trapped hydrogen concentration was 4.02 mol m^{-3}, equivalent to 58 % of the total absorbed hydrogen.

For the three 980 DP steels, 980 DP, 980 DP-GI (650 MPa YS) and 980 DP-GI (700 MPa YS) steel, with increasing yield strength and decreasing grain size, the calculated reversible hydrogen trap site density increased from 1.88×10^{18} sites cm^{-3} to 2.42×10^{18} sites cm^{-3} and to 3.30×10^{18} sites cm^{-3}, and the corresponding percentage of trapped hydrogen in total absorbed hydrogen also increased from 54 % to 58 % and to 64 %. This was consistent with the results of the decreased diffusion coefficients for these three steel grades, caused by more hydrogen traps with finer grain sizes.

For 980 DP and 1200 DP-GI, which had similar grain sizes, the trap site density for 1200 DP-GI was 2.26×10^{18} sites cm^{-3}, 20 % higher than that of 1.88×10^{18} sites cm^{-3} for 980 DP steel, attributed to the higher martensite content that provided more trap sites in 1200 DP-GI.

The density of reversible hydrogen trap sites for 980 QP steel was 5.91×10^{17} sites cm^{-3} and was significantly lower, by a factor of 3 to 4, than that for the 980 DP steels. This was considered to result from the presence of retained austenite, acting as more potent hydrogen traps, and that the hydrogen trapped in austenite was not emptied during the complete decay transients. Sojka et al. [37] found that TRIP 800 steel absorbed much more hydrogen than other AHSS due to the higher retained austenite content. Zhu et al. [38], observed the hydrogen trap sites in Q&P steels directly using three-dimensional atom probe tomography (3DAPT). They found that austenite contained three times more hydrogen than martensite and the hydrogen trapping in ferrite was low due to the small solubility and fast diffusivity of hydrogen in the bcc iron structure. They further claimed that this retained austenite with high concentration of hydrogen could be detrimental source when the martensite transformation occurred, leading to susceptibility of the steels to hydrogen embrittlement, as also stated in other studies [39, 40]. Therefore, the stability of retained austenite was important to reduce the martensite transformation so that the high concentration of hydrogen in austenite would not assist the HE of the steel [41-43]. In addition, the size and morphology of the retained austenite were also stated to be decisive in terms of the resistance to HE [37, 44]. However, the stability and morphology of retained austenite are beyond the scope of this study.

5. Discussion

5.1 Charging conditions

In this study, the purpose of the pre-charging was (i) to condition the surface to a relatively stable state, which minimized the surface effect to allow reproducible permeation transients; and (ii) to fill all the irreversible and reversible hydrogen traps. During the pre-charging, it is considered that all traps were filled at random, but that the hydrogen in irreversible traps cannot escape. Thus with sufficient pre-charging time, all the irreversible traps are filled and reversible traps are in equilibrium with the diffusible hydrogen. In subsequent permeation transients, only reversible traps are evaluated.

The successive partial transients did not allow complete dehydrogenation, and thus the irreversible traps remained saturated during the transients. The charging conditions for

partial transients in this study correspond to the charging conditions for hydrogen embrittlement tests, and the evaluated density of reversible hydrogen trap sites correspond to each charging condition.

The complete decay transients, in contrast, allowed dehydrogenation on the hydrogen entry side. However, due to the high binding energy of irreversible hydrogen traps, ~ 56 kJ mol^{-1} [45], the irreversible hydrogen traps were unlikely to be emptied at a temperature of 25 ± 2 ℃. Thus, the trap site density evaluated from the complete decay in this study was also the density of reversible hydrogen trap sites.

5.2 Diffusion coefficients

Fig. 10 presents the measured diffusion coefficient for each steel at the different applied potentials from the transient loop. The error bars in Fig. 10 depict the standard deviation for the measured D_{eff} values. Fig. 10 and Table 3 indicate that, for the DP steels studied in this research, the values for effective diffusion coefficient were in the range of 0.5 × 10^{-6} cm^2 s^{-1} ~ 2.1 × 10^{-6} cm^2 s^{-1}, consistent with those from literature [46-49]. For 980 QP steel, the effective diffusion coefficient varied from 3 × 10^{-7} cm^2 s^{-1} to 7 × 10^{-7} cm^2 s^{-1}, in agreement with the range of 0.3 × 10^{-7} cm^2 s^{-1} to 6 × 10^{-7} cm^2 s^{-1} from other studies [41, 44, 47], despite the fact that different methods were used to determine the diffusion coefficient, which would lead to a variance of the values. For instance, Yang et al. [41] used two methods, the time lag method and the breakthrough method, to determine the hydrogen diffusion coefficient of their Q&P steels. The results obtained from both methods had a difference of least a factor of 2.

Fig. 10 and Table 3 further indicate that, for each steel, the diffusion coefficient increased with increasingly negative potential from – 1.100 $V_{Hg/HgO}$ to – 1.700 $V_{Hg/HgO}$ for both the rise and decay transients. For example, at – 1.100 $V_{Hg/HgO}$, the value of hydrogen diffusion coefficient for 980 DP-GI (650 MPa YS) was 0.76 × 10^{-6} cm^2 s^{-1}, whilst at – 1.700 $V_{Hg/HgO}$, the D_{eff} value was 1.36 × 10^{-6} cm^2 s^{-1}. There was a similar trend for each steel. This trend was attributed to more potent trapping at a less negative charging potential. At a less negative potential, less hydrogen was produced and entered into the specimen, fewer traps were full, more traps were filled during the transient, and consequently the diffusion coefficient was lower. In comparison, there was a larger amount of generated hydrogen at more negative potentials, more hydrogen traps were full, and the empty traps had less influence on hydrogen diffusion coefficient.

5.3 Trap site densities

Table 4 indicates that that, for each of the DP and Q&P steels, with increasingly negative charging potential, from -1.100 $V_{Hg/HgO}$ to -1.700 $V_{Hg/HgO}$, the corresponding reversible hydrogen trap site density decreased. The increase in the effective diffusion coefficient with increasingly negative potential is attributed to a less potent trapping effect at a more negative potential. From -1.700 $V_{Hg/HgO}$ to -1.600 $V_{Hg/HgO}$, the trapped hydrogen corresponded to 1 % or less of the total absorbed hydrogen, and thus, the repeated transient from -1.600 $V_{Hg/HgO}$ to -1.700 $V_{Hg/HgO}$ could be used to determine the lattice diffusion coefficient. Furthermore, the effective diffusion coefficient decreased from the value of the lattice diffusion coefficient as the trap effect became greater.

Tables 3 and 4 indicate that, for the three 980 DP steel grades, with increasing yield strength and decreasing grain size, the values of the lattice diffusion coefficient and the values of the effective diffusion coefficient decreased slightly, but the hydrogen trap density increased from 980 DP to 980 DP-GI (650 MPa YS) and then decreased to 980 DP-GI (700 MPa YS). Thus the decrease in effective diffusion coefficient in this series is attributed to a combination of the decrease in lattice diffusion coefficient and the increase in trapping effect.

The values of the diffusion coefficient of 1200 DP-GI steel were somewhat lower than that of the 980 DP steel. The lower lattice diffusion coefficient of 1200 DP-GI is attributed to the lower ferrite content. The small decrease with decreasingly negative potential is attributed to a slightly increased trapping effect; the trap density for 1200 DP-GI is similar to that of 980 DP-GI (700 MPa YS).

The lattice and effective diffusion coefficients for 980 QP steel were similar to those of 980 DP-GI (700 MPa YS). The lower lattice diffusion coefficient is attributed to the higher carbon content of the 980 QP steel. The similar decrease of effective diffusion coefficient with decreasingly negative potential is attributed to a similar trap effect.

In summary, the values of the effective diffusion coefficient for each steel could be explained in terms of a trapping effect.

5.3.1 Partial decay transients

The density of reversible hydrogen trap site was evaluated using the two methods: (i) the Oriani-Dong model [25], and the permeation curve method [27], Table 4. The values

were comparable, however the values of total trap density evaluated by the permeation curve method were somewhat smaller than those evaluated using Oriani-Dong model. This may be attributed to the followed reasons:

(i) N_L. This study, due to the lack of available data for DP and Q&P steels, used the value of 7.2×10^{22} sites cm^{-3}, adopted from the reported value for α-Fe [16]. Since N_t is directly proportional to N_L, an error in N_L directly causes a similar error in the density of trap sites.

(ii) E_b. The trap binding energy characterises the trap type. Each trap has a different binding energy. In this study one type of reversible trap was assumed. A value of 28.9 kJ mol^{-1} was assumed for E_b. However, more than one type of reversible trap was expected in the DP and Q&P steels, especially the Q&P steel because of the retained austenite. Thus, using a single value of E_b would also lead to the different calculated values.

Nevertheless, the results from both methods showed good consistency: (i) the densities of reversible hydrogen trap sites, N_t and N_t^*, exhibited the same trend that the values were lower at a more negative potential, (ii) the trapped hydrogen was a lower percentage of the total absorbed hydrogen at a more negative potential, and (iii) the reversible hydrogen trap density values evaluated between -1.700 $V_{Hg/HgO}$ to -1.100 $V_{Hg/HgO}$ using these two methods were similar in magnitude of ~10^{18} sites cm^{-3} for all the steels, although there was a difference of three times for 980 QP steel. Such a difference was not higher than that from the literature [29].

5.3.2 Complete decay transients

Tables 4 and 5 present values of the reversible hydrogen trap site density, evaluated using the permeation curve method, (i) for partial decay transients between -1.700 $V_{Hg/HgO}$ to -1.100 $V_{Hg/HgO}$, and (ii) for complete decay transients from -1.700 $V_{Hg/HgO}$ to the open circuit potential (ocp).

The trap site density from complete decay was significantly higher than that from partial decay transients for each of the studied steels. For example, for 980 DP-GI (650 MPa YS) steel, N_t^* was 11.1×10^{17} sites cm^{-3} between -1.700 $V_{Hg/HgO}$ to -1.100 $V_{Hg/HgO}$, whereas N_t^* was 24.2×10^{17} sites cm^{-3}, more than 100 % higher, from the complete decay. Correspondingly, the trapped hydrogen, evaluated from the complete decay, accounted for 58 % of the total absorbed hydrogen, whilst from partial decay transients, the percentage was

significantly lower. Especially for the most negative charging conditions, from -1.700 $V_{Hg/HgO}$ to -1.600 $V_{Hg/HgO}$, the trapped hydrogen was 0.5 % of the total amount of hydrogen. This was attributed to the less significant trapping effect at more negative charging potentials, as was also found by Liu and Atrens [29].

Reversible traps have a significant influence on hydrogen diffusion and on hydrogen embrittlement susceptibility. The permeation curve method is a useful way of estimation the reversible trap site density. However, when using this method, the evaluated value from a complete decay involves all the reversible traps and is higher than that evaluated from partial decay transients, which only involved the reversible traps under the particular charging conditions. Thus, for understanding the reversible hydrogen traps that influence the hydrogen diffusion behaviour under particular charging conditions, the Oriani-Dong model and permeation curve method are both useful.

5.4 Comparison with literature

Table 6 shows the values of reversible hydrogen trap density determined through permeability experiments from the literature [25, 27-29, 44, 45, 47, 50], where t_L is the lattice breakthrough time and t_L* is the lattice time lag, both related to the lattice diffusion coefficient, D_L, t_T is the breakthrough time with trapping and t_T* is time lag in the presence of trapping, C_a is the average hydrogen concentration at steady state, and the other symbols have the same meaning as in this paper.

The magnitude of reversible hydrogen trap densities ranged from 10^{12} sites cm^{-3} to 10^{26} sites cm^{-3} for different steels and using various mathematic models. The values measured herein are in the middle of this range.

Liu and Atrens [29] used an approach similar to that used herein, and evaluated similar trap densities to those estimated herein. Fallahmohammadi et al. [28] and Frappart et al. [45] used similar models, both adopted from Kumnick and Johnson [51] and related to time lag or breakthrough time, to calculate the trap site density in their steels. Both studies estimates similar values of 10^{19} sites cm^{-3}, and similar values were obtained by [24, 52, 53], and were somewhat higher than the values estimated herein. This difference in values may be attributed to the intrinsic difference of the materials used in these studies and difference in methods for calculating the trap site density.

Zhu et al. [44] determined the density of hydrogen traps in quenching and partitioning (Q&P) steels with different heat treatments. The densities for all their steels were of similar

magnitude of 10^{21} sites cm^{-3}. However, the model they used to calculate hydrogen trap density did not involve the trap binding energy, E_b, and was also different from the Oriani-Dong model [25] as used herein this paper.

Zakroczymski [27] determined the mount of trapped hydrogen using complete permeation decay curve and obtained around 10^{-7} mol cm^{-2} of trapped hydrogen from the hydrogen detection side. By using Eq. (6) and (7) in this paper, we converted the amount of hydrogen to trap site density and obtained an estimation of around 10^{13} sites cm^{-3}, as shown in Table 6. This value was lower than those in our study by a few orders of magnitude. This is within expectation, since a much lower hydrogen trap density is expected in the Armco iron used in the study of Zakroczymski [27].

In other research [25, 29, 47, 50] using similar model as the Oriani-Dong model [25] as in this paper, the reversible hydrogen trap density values ranged from 10^{12} sites cm^{-3} to 10^{26} sites cm^{-3}. Table 6 documents that different values have been assigned to the parameters in this model. For example, Liu et al. [29] used the value for N_L obtained from a quenched and tempered martensitic steel, whereas other researchers [25, 47, 50] used the N_L values for α-Fe or the tetrahedral site density in bcc Fe at room temperature. The value of N_L for α-Fe was also used in this study. Araújo et al. [16] asserted that the value for N_L depended on the type of metal being analysed. As a consequent, different values were assigned to this parameter and contributed to the variation of the calculated trap site density. The same would happen when different values were assigned to D_L or E_b, as also mentioned above in section 5. In addition, the Oriani-Dong model [25] also involved the effective diffusion coefficient. The diffusion coefficient was influenced by the sub-surface hydrogen concentration and thus by the charging condition [29, 45].

Nevertheless, the values of trap site density obtained using the two methods in this study were comparable and were around 10^{18} sites cm^{-3}, were consistent with the results of Liu et al. [29] and were within the range of the values from the literature [24, 25, 27-29, 44, 45, 47, 50, 52, 53].

5.5 Microstructure

Table 1 and Fig. 3 indicate that the microstructure of the DP steels consisted mainly of ferrite and martensite whereas the microstructure of the Q&P steel consisted of ferrite, bainite and retained austenite.

Table 1 and 2 indicate that, for the three 980 DP grades of steels, from 980 DP to 980 DP-GI (650 MPa YS) and to 980 DP-GI (700 MPa YS), the yield strength increased, the relative amount of ferrite decreased, and the grain size decreased. The decreasing grain size can be related to grain refinement by the increasing Ti alloying content, and is consistent with the increasing yield strength.

1200 DP-GI and 980 DP steels had similar grain sizes. The higher strength of the 1200 DP steel was attributed to (i) the higher amount of martensite, which was 74% compared with 60% for 980 DP steel and thus the lower volume fraction of ferrite, and (ii) the slightly higher carbon concentration, which is expected to produce a stronger martensite.

980 QP steels had 39% of soft ferrite and 53% of hard bainite and 8% of retained austenite, which had a hydrogen diffusion coefficient much lower than that of ferrite, and a solubility of hydrogen higher than ferrite and martensite [47, 54].

During pre-charging, it took the hydrogen about 315 s, 1235 s, 1503 s, 1184 s and 810 s to breakthrough to the other side of the specimen of 980 DP, 980 DP-GI (650 MPa YS), 980 DP-GI (700 MPa YS), 1200 DP-GI, and 980 QP, respectively. Increased breakthrough time indicates a lower effective diffusion coefficient, which could be caused by a larger trapping effect, or there could be also a contribution from the lattice diffusion coefficient. The breakthrough times roughly correlate with the total density of trap sites as evaluated in Table 5, except that the trap densities are not sufficiently high for 980 QP, in which case there is assumed to be a significant influence from the low lattice diffusion coefficient for 980 QP, see Table 3. Fig. 4 shows that it took a shorter time of peaking for the 980 DP-GI (650 MPa YS) and 980 DP-GI (700 MPa YS). This is attributed to the surface of these steel samples, which had been galvanized and the galvanizing was removed by grinding and polishing. The reason for the different times to reach steady-state current density of the different steels was attributed to the differences in the way the surfaces reacted to the cathodic charging. The values of the steady-state current density of different steels correspond to the values of i_∞ at the end of transient from -1.700 $V_{Hg/HgO}$ to -1.600 $V_{Hg/HgO}$ in Table 4, which provides corresponding values for C_T and C_L.

Tables 1, 2 and 3 indicate that, for the three 980 DP steel grades, with increasing yield strength, decreasing ferrite content, and decreasing grain size, the values of the lattice diffusion coefficient decreased slightly from 2.07×10^{-6} cm^2 s^{-1} to 1.58×10^{-6} cm^2 s^{-1} to 0.75×10^{-6} cm^2 s^{-1}. This decrease in the lattice diffusion coefficient is attributed to the decreasing fraction of ferrite in the microstructure. It is expected that the diffusion coefficient of the

ferrite dominates the diffusion coefficient of the steel, because the diffusion coefficient of the martensite is much lower due to its highly distorted lattice.

The value of the diffusion coefficient of 1200 DP-GI steel was somewhat lower than that of the 980 DP steel. The lower lattice diffusion coefficient of 1200 DP-GI is attributed to the lower ferrite content.

The lattice diffusion coefficient values for 980 QP steel was lower than that of 980 DP-GI (700 MPa YS) attributed to the higher carbon content of the 980 QP steel.

6. Conclusions

1. The values of reversible hydrogen trap site density and the proportion of the reversibly trapped hydrogen for the DP and Q&P steels indicated that (i) the trapping effect was less significant at a more negative potential, and (ii) the lattice diffusion coefficient of hydrogen could be measured from the partial transients at the most negative potentials.
2. The values of the effective diffusion coefficient measured in this work were consistent with literature values.
3. The densities of reversible hydrogen trap sites from complete decays were ~ 2×10^{18} sites cm^{-2} and were a factor of two higher than those from partial decay transients between -1.700 $V_{Hg/HgO}$ and -1.100 $V_{Hg/HgO}$.
4. The densities of reversible hydrogen trap sites estimated in this work were consistent with literature values.
5. The values of hydrogen lattice diffusion coefficient and values of the reversible trap site density were within fairly narrow ranges for the steels studied, reflecting the fact that the steels were quite similar.

ACKNOWLEDGEMENTS

This research is supported by the Baosteel-Australia Joint Research & Development Centre (BAJC) Grant, BA13037, with linkage to Baoshan Iron and Steel Co., Ltd of China.

7. References

[1] D Bhattacharya, Developments in Advanced High Strength Steels, Proceedings of Proceedings of the Joint International Conference of HSLA Steels, Sanya, 2005, 70-73.
[2] X Zhu, Z Ma and L Wang, Current Status of Advanced High Strength Steel for Auto-making and its Development in Baosteel, Avaliable from www.baosteel.com, Access on November 26, 2014.
[3] WorldAutoSteel, Advanced high-strength steels application guidelines version 5.0, Available from http://www.worldautosteel.org/, Access on 2014.
[4] BC De Cooman, L Chen, HS Kim, Y Estrin, SK Kim and H Voswinckel, State-of-the-Science of High Manganese TWIP Steels for Automotive Applications, Microstructure and Texture in Steels, Charpter 10, p. 165-183, Springer, London, 2009.
[5] BaoSteel, BaoSteel automotive advanced high strength steels, Avaliable from www.baosteel.com, Access on November 12, 2014 (2013).
[6] VF Zackay, ER Parker, D Fahr and R Busch, THE ENHANCEMENT OF DUCTILITY IN HIGH-STRENGTH STEELS, ASM TRANS QUART 60 (1967) 252-259.
[7] M Chen, R Wu, H Liu, L Wang, J Shi, H Dong and X Jin, An ultrahigh strength steel produced through deformation-induced ferrite transformation and Q&P process, Sci China Technol Sci. 55 (2012) 1827-1832.
[8] DV Edmonds, K He, FC Rizzo, BC De Cooman, DK Matlock and JG Speer, Quenching and partitioning martensite—A novel steel heat treatment, Mater Sci Eng A. 438-440 (2006) 25-34.
[9] MJ Santofimia, L Zhao and J Sietsma, Overview of Mechanisms Involved During the Quenching and Partitioning Process in Steels, Metall Mater Trans A. 42 (2011) 3620-3626.
[10] DK Matlock and JG Speer, Third Generation of AHSS: Microstructure Design Concepts, Microstructure and Texture in Steels, Charpter 11, p. 185-205, Springer London, 2009.
[11] G Lovicu, M Bottazzi, F D'Aiuto, M De Sanctis, A Dimatteo, C Santus and R Valentini, Hydrogen Embrittlement of Automotive Advanced High-Strength Steels, Metall Mater Trans A. 43 (2012) 4075-4087.
[12] M Robinson and P Kilgallon, Hydrogen embrittlement of cathodically protected high-strength, low-alloy steels exposed to sulfate-reducing bacteria, Corrosion. 50 (1994) 626-635.
[13] A Lasia and D Grégoire, General model of electrochemical hydrogen absorption into metals, J Electrochem Soc. 142 (1995) 3393-3399.
[14] D Hardie, EA Charles and AH Lopez, Hydrogen embrittlement of high strength pipeline steels, Corros Sci. 48 (2006) 4378-4385.
[15] M Devanathan and Z Stachurski, The adsorption and diffusion of electrolytic hydrogen in palladium, Proceedings of the Royal Society of London. Series A. Mathematical and Physical Sciences. 270 (1962) 90-102.
[16] DF Araújo, EO Vilar and J Palma Carrasco, A critical review of mathematical models used to determine the density of hydrogen trapping sites in steels and alloys, Int J Hydrogen Energy. 39 (2014) 12194-12200.
[17] J Lee and S Lee, Hydrogen trapping phenomena in metals with BCC and FCC crystals structures by the desorption thermal analysis technique, Surf Coat Technol. 28 (1986) 301-314.
[18] P Castaño Rivera, VP Ramunni and P Bruzzoni, Hydrogen trapping in an API 5L X60 steel, Corros Sci. 54 (2012) 106-118.
[19] AH Krom and A Bakker, Hydrogen trapping models in steel, Metall Mater Trans. 31 (2000) 1475-1482.

[20] M Luppo and J Ovejero-Garcia, The influence of microstructure on the trapping and diffusion of hydrogen in a low carbon steel, Corros Sci. 32 (1991) 1125-1136.
[21] J Rehrl, K Mraczek, A Pichler and E Werner, The Impact of Nb, Ti, Zr, B, V, and Mo on the Hydrogen Diffusion in Four Different AHSS/UHSS Microstructures, steel research international. 85 (2014) 336-346.
[22] J Hirth, Effects of hydrogen on the properties of iron and steel, Metall Trans A. 11 (1980) 861-890.
[23] A McNabb and P Foster, A new analysis of the diffusion of hydrogen in iron and ferritic steels, Trans. Aime. 227 (1963) 618.
[24] RA Oriani, The diffusion and trapping of hydrogen in steel, Acta Metall. 18 (1970) 147-157.
[25] CF Dong, ZY Liu, XG Li and YF Cheng, Effects of hydrogen-charging on the susceptibility of X100 pipeline steel to hydrogen-induced cracking, Int J Hydrogen Energy. 34 (2009) 9879-9884.
[26] A Atrens, D Mezzanotte, N Fiore and M Genshaw, Electrochemical studies of hydrogen diffusion and permeability in Ni, Corros Sci. 20 (1980) 673-684.
[27] T Zakroczymski, Adaptation of the electrochemical permeation technique for studying entry, transport and trapping of hydrogen in metals, Electrochim Acta. 51 (2006) 2261-2266.
[28] E Fallahmohammadi, F Bolzoni and L Lazzari, Measurement of lattice and apparent diffusion coefficient of hydrogen in X65 and F22 pipeline steels, Int J Hydrogen Energy. 38 (2013) 2531-2543.
[29] Q Liu and A Atrens, Reversible hydrogen trapping in a 3.5NiCrMoV medium strength steel, Corros Sci. 96 (2015) 112-120.
[30] E562-08, Standard Test Method for Determining Volume Fraction by Systematic Manual Point Count, 2008.
[31] E-112, Standard test methods for determining average grain size, 2010.
[32] GF Vander Voort, Metallography, principles and practice, ASM International, 1984.
[33] Q Liu, AD Atrens, Z Shi, K Verbeken and A Atrens, Determination of the hydrogen fugacity during electrolytic charging of steel, Corros Sci. 87 (2014) 239-258.
[34] J Flis, T Zakroczymski, V Kleshnya, T Kobiela and R Duś, Changes in hydrogen entry rate and in surface of iron during cathodic polarisation in alkaline solutions, Electrochim Acta. 44 (1999) 3989-3997.
[35] J McBreen, L Nonis and W Beck, A method for determination of the permeation rate of hydrogen through metal membranes, J Electrochem Soc. 113 (1966) 1218-1222.
[36] J Venezuela, Q Liu, M Zhang, Q Zhou and A Atrens, The influence of hydrogen on the mechanical and fracture properties of some martensitic advanced high strength steels studied using the linearly increasing stress test, Corros Sci. 99 (2015) 98-117.
[37] J Sojka, V Vodárek, I Schindler, C Ly, M Jérôme, P Váňová, N Ruscassier and A Wenglorzová, Effect of hydrogen on the properties and fracture characteristics of TRIP 800 steels, Corros Sci. 53 (2011) 2575-2581.
[38] X Zhu, W Li, H Zhao, L Wang and X Jin, Hydrogen trapping sites and hydrogen-induced cracking in high strength quenching & partitioning (Q&P) treated steel, Int J Hydrogen Energy. 39 (2014) 13031-13040.
[39] J Ronevich, B De Cooman, J Speer, E De Moor and D Matlock, Hydrogen effects in prestrained transformation induced plasticity steel, Metall Mater Trans A. 43 (2012) 2293-2301.
[40] JH Ryu, YS Chun, CS Lee, HKDH Bhadeshia and DW Suh, Effect of deformation on hydrogen trapping and effusion in TRIP-assisted steel, Acta Mater. 60 (2012) 4085-4092.

[41] J Yang, F Huang, Z Guo, Y Rong and N Chen, Effect of retained austenite on the hydrogen embrittlement of a medium carbon quenching and partitioning steel with refined microstructure, Mater Sci Eng A. 665 (2016) 76-85.
[42] T Hojo, J Kobayashi, T Kajiyama and K Sugimoto, Effects of Alloying Elements on Impact Properties of Ultra High-Strength TRIP-Aided Bainitic Ferrite Steels, Res Rep Tsuyama Technical College. 52 (2010) 9-16.
[43] X Zhu, W Li, H Zhao and X Jin, Effects of cryogenic and tempered treatment on the hydrogen embrittlement susceptibility of TRIP-780 steels, Int J Hydrogen Energy. 38 (2013) 10694-10703.
[44] X Zhu, K Zhang, W Li and X Jin, Effect of retained austenite stability and morphology on the hydrogen embrittlement susceptibility in quenching and partitioning treated steels, Mater Sci Eng A. 658 (2016) 400-408.
[45] S Frappart, X Feaugas, J Creus, F Thebault, L Delattre and H Marchebois, Study of the hydrogen diffusion and segregation into Fe–C–Mo martensitic HSLA steel using electrochemical permeation test, Journal of Physics and Chemistry of Solids. 71 (2010) 1467-1479.
[46] J Malina, A Begić Hadžipašić and Š Nižnik, Electrochemical corrosion and hydrogen diffusivity in dual-phase steel, Proceedings of 2nd International Conference Corrosion and Material Protection, EFC Event, 2010,
[47] A Begić Hadžipašić, J Malina and M Malina, The influence of microstructure on hydrogen diffusion and embrittlement of multiphase fine-grained steels with increased plasticity and strength, Chem Biochem Eng Q. 25 (2011) 159-169.
[48] T Depover, E Wallaert and K Verbeken, Fractographic analysis of the role of hydrogen diffusion on the hydrogen embrittlement susceptibility of DP steel, Mater Sci Eng A. 649 (2016) 201-208.
[49] M Koyama, CC Tasan, E Akiyama, K Tsuzaki and D Raabe, Hydrogen-assisted decohesion and localized plasticity in dual-phase steel, Acta Mater. 70 (2014) 174-187.
[50] AJ Haq, K Muzaka, DP Dunne, A Calka and EV Pereloma, Effect of microstructure and composition on hydrogen permeation in X70 pipeline steels, Int J Hydrogen Energy. 38 (2013) 2544-2556.
[51] A Kumnick and H Johnson, Deep trapping states for hydrogen in deformed iron, Acta Metall. 28 (1980) 33-39.
[52] A Turnbull, M Carroll and D Ferriss, Analysis of hydrogen diffusion and trapping in a 13% chromium martensitic stainless steel, Acta Metall. 37 (1989) 2039-2046.
[53] A Perujo, E Serra, S Alberici, S Tominetti and J Camposilvan, Hydrogen in the martensitic DIN 1.4914: a review, Journal of alloys and compounds. 253 (1997) 152-155.
[54] M Koyama, E Akiyama and K Tsuzaki, Hydrogen embrittlement in a Fe–Mn–C ternary twinning-induced plasticity steel, Corros Sci. 54 (2012) 1-4.

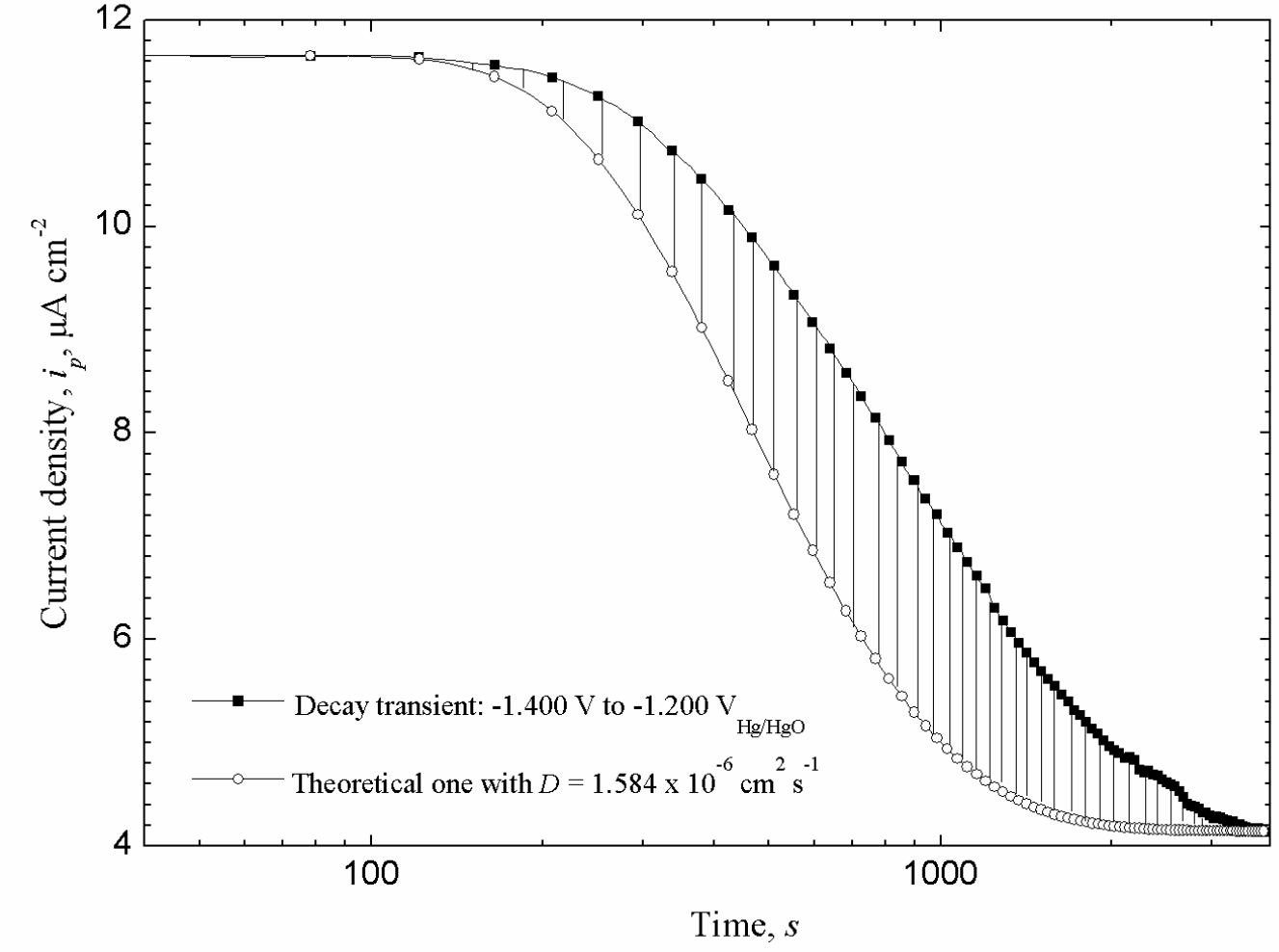

Fig. 1 The typical area difference (shaded part) between the integration of the permeation curve and the theoretical one for a decay transient for a 980 DP-GI (650 MPa YS) steel hydrogen charged in 0.1 M NaOH solution.

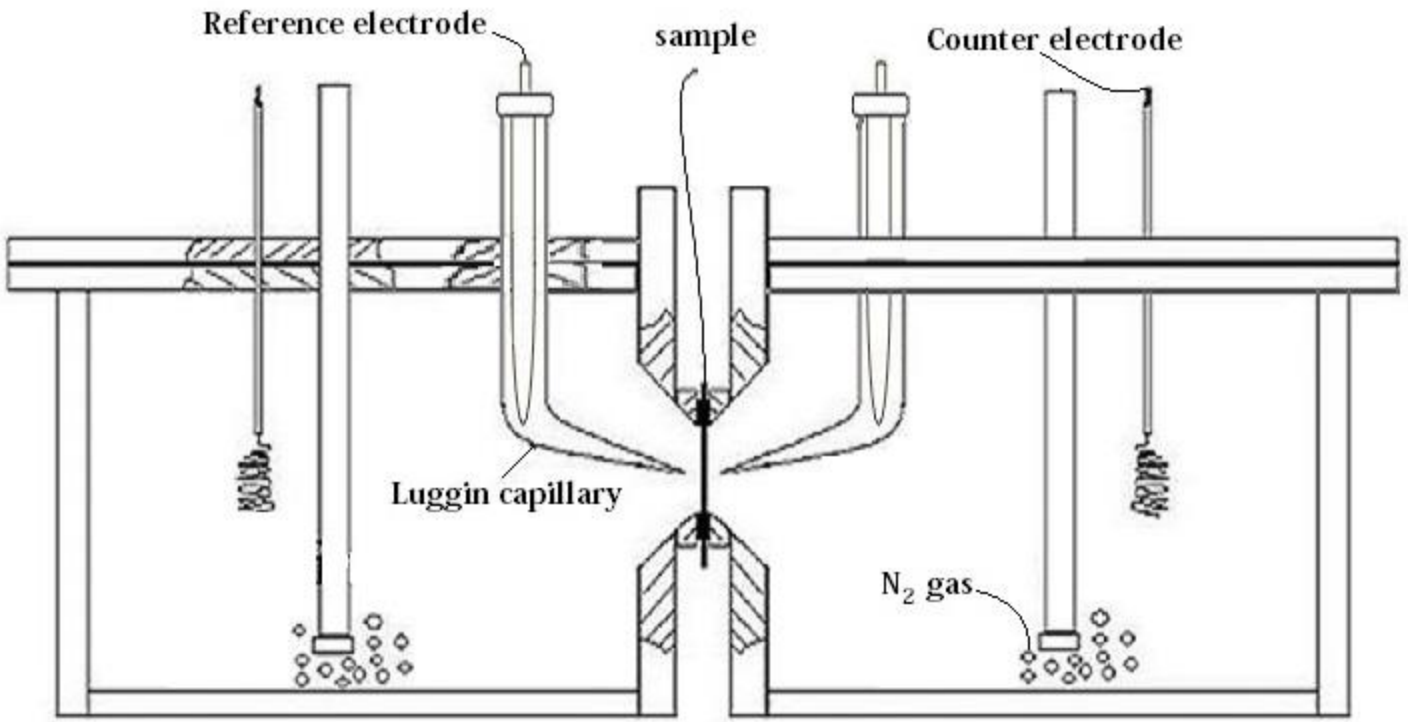

Fig. 2 Schematic of permeability cell

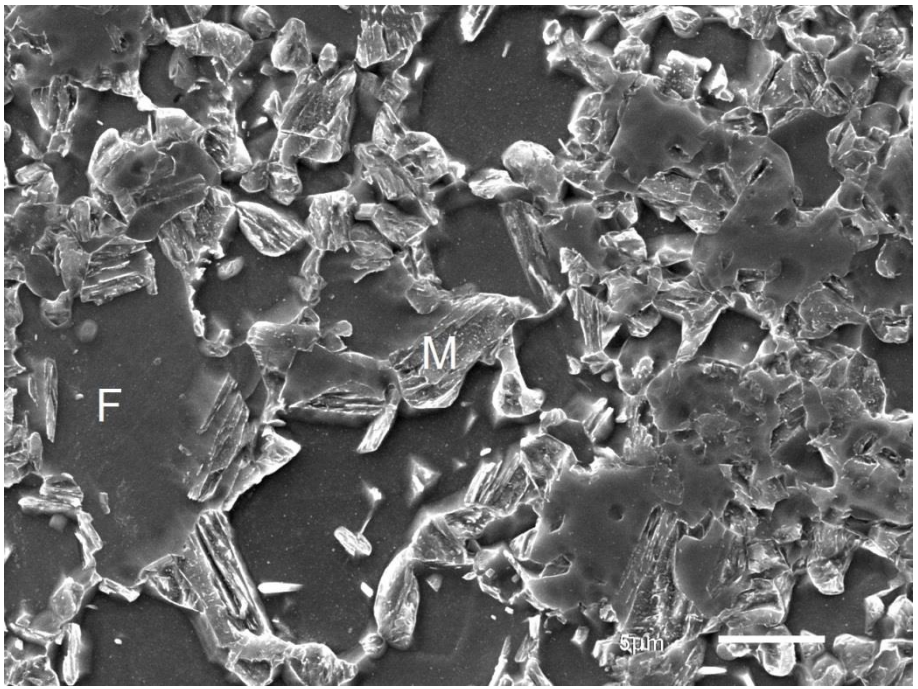

(a)

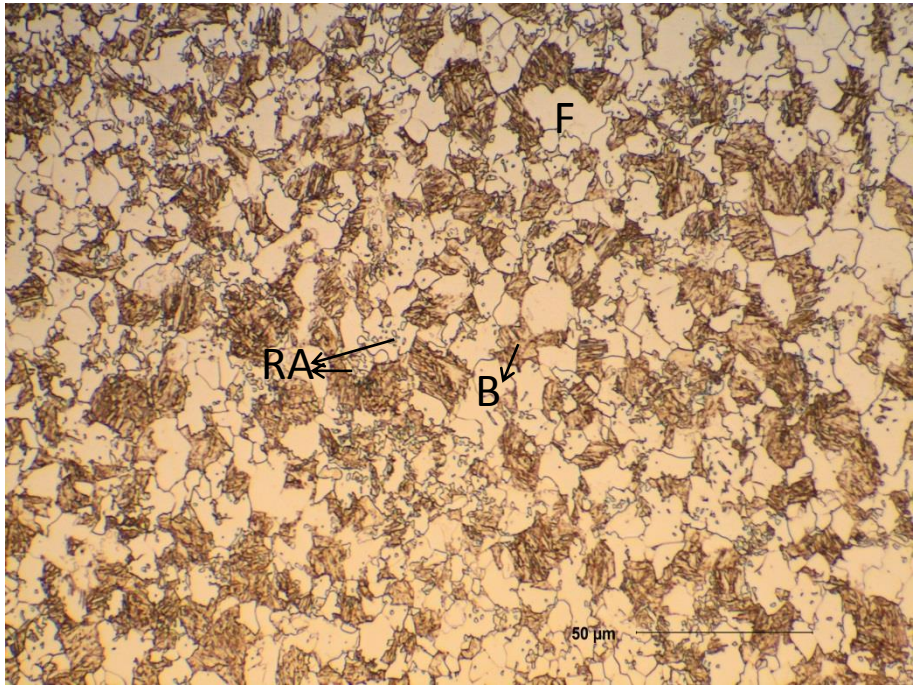

(b)

Fig. 3 Microstructures of (a) 980 DP steel observed under SEM and (b) 980 QP steel viewed with light microscope. M stands for martensite, F is for ferrite, B is for bainite and RA refers to retained austenite.

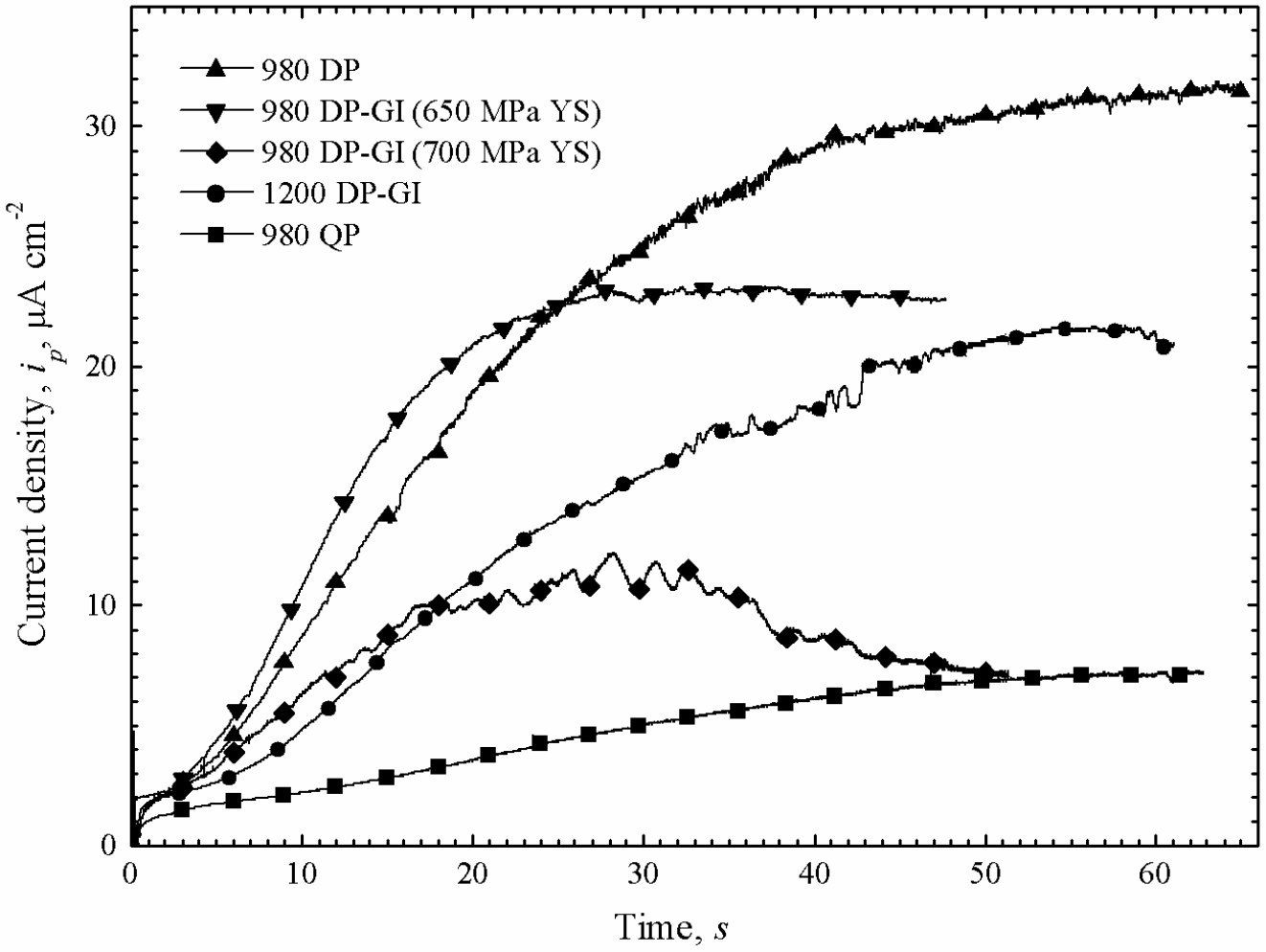

Fig. 4 Hydrogen permeation current density *vs.* time for the steels during long time pre-charging in 0.1 M NaOH solution at -1.600 $V_{Hg/HgO}$.

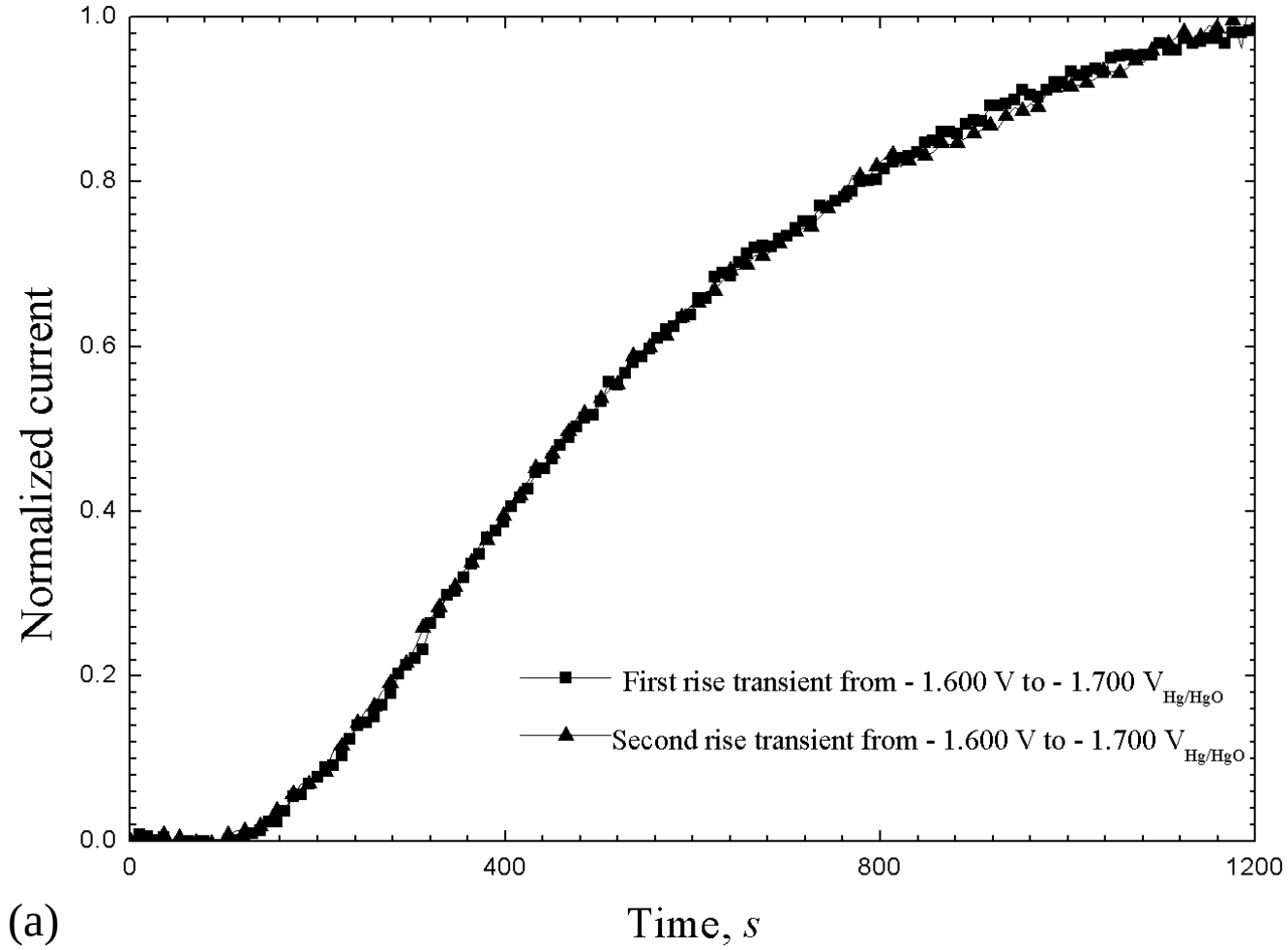
1.0
0.8
0.6
0.4
0.2
0.0
Normalized current
0
400
800
1200
Time, s
First rise transient from - 1.600 V to - 1.700 V Hg/HgO
Second rise transient from - 1.600 V to - 1.700 V Hg/HgO

(a)

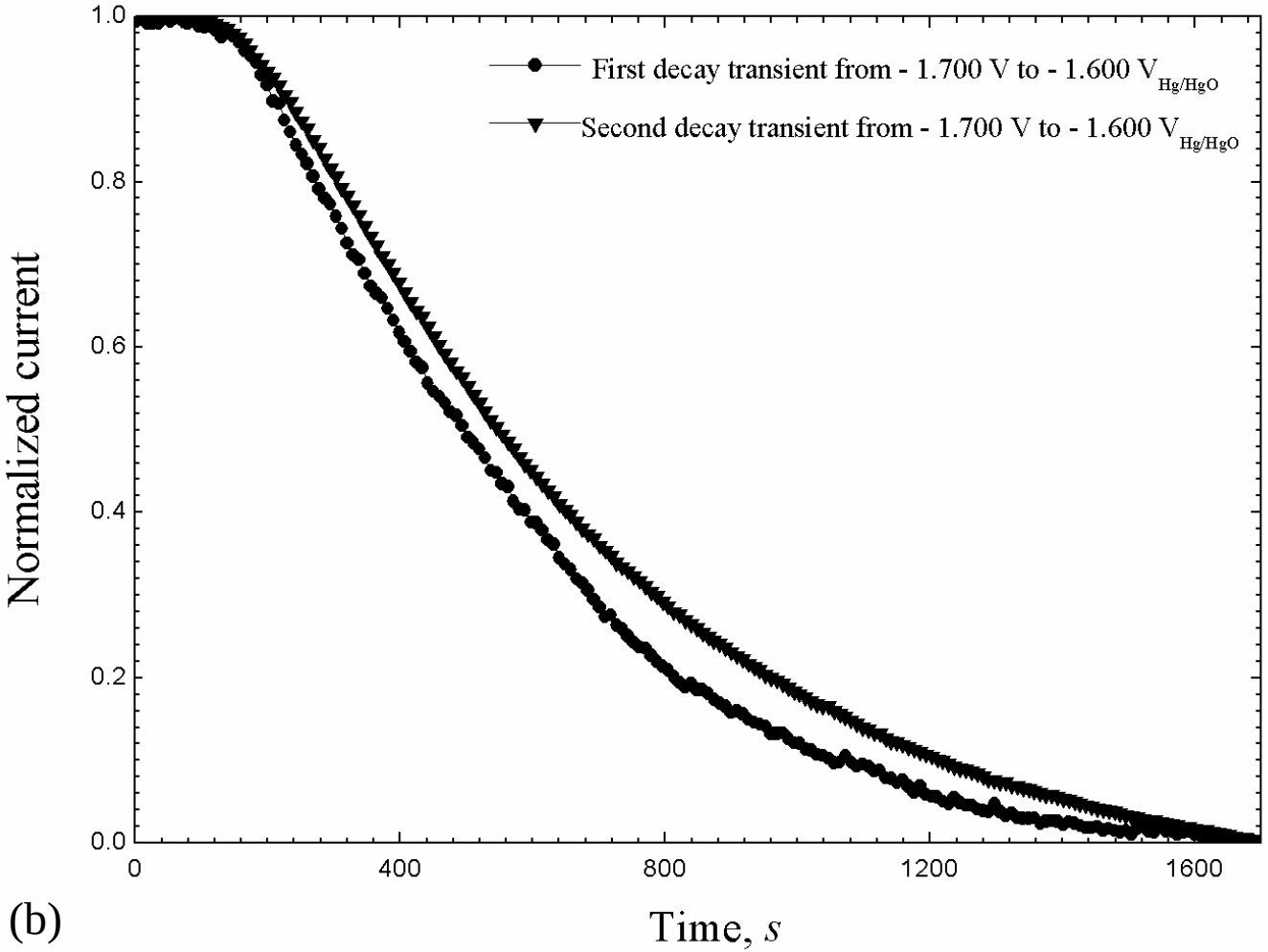

Fig. 5 The normalized current (as defined by Eq. (8) and (9)) of two sequential (a) rise and (b) decay transients between -1.700 $V_{Hg/HgO}$ and -1.600 $V_{Hg/HgO}$ for 980 DP-GI (645 MPa YS) in 0.1 M NaOH solution. For a rise transient, the normalised current is equal to (the measured current minus the initial current) divided by (the difference between the final current and the initial current). For a decay transient, the normalised current is equal to (the initial current minus the measured current) divided by (the difference between the initial current and the final current).

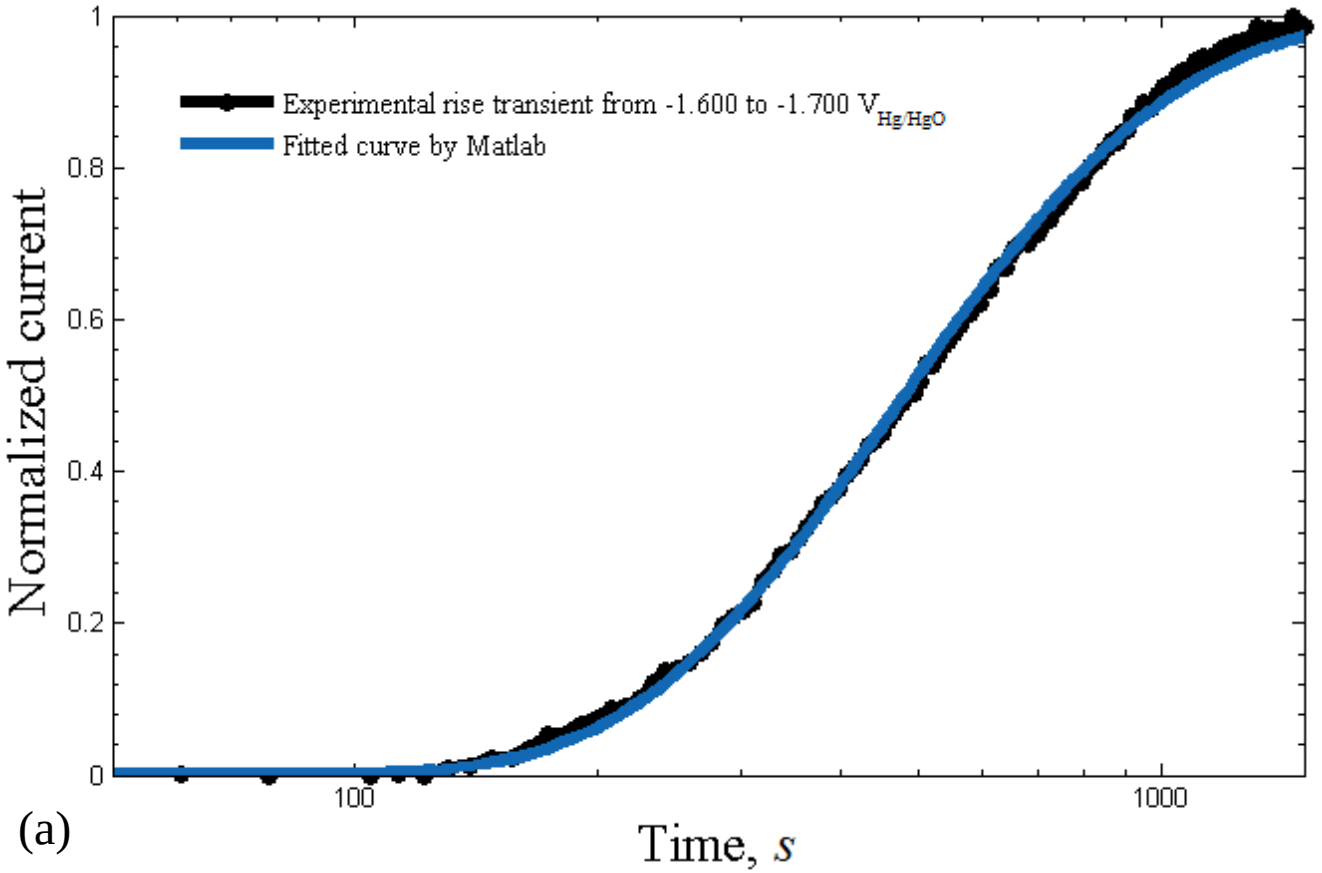
Experimental rise transient from -1.600 to -1.700 V Hg/HgO
Fitted curve by Matlab
Normalized current
Time, s
0
0.2
0.4
0.6
0.8
1
100
1000

(a)

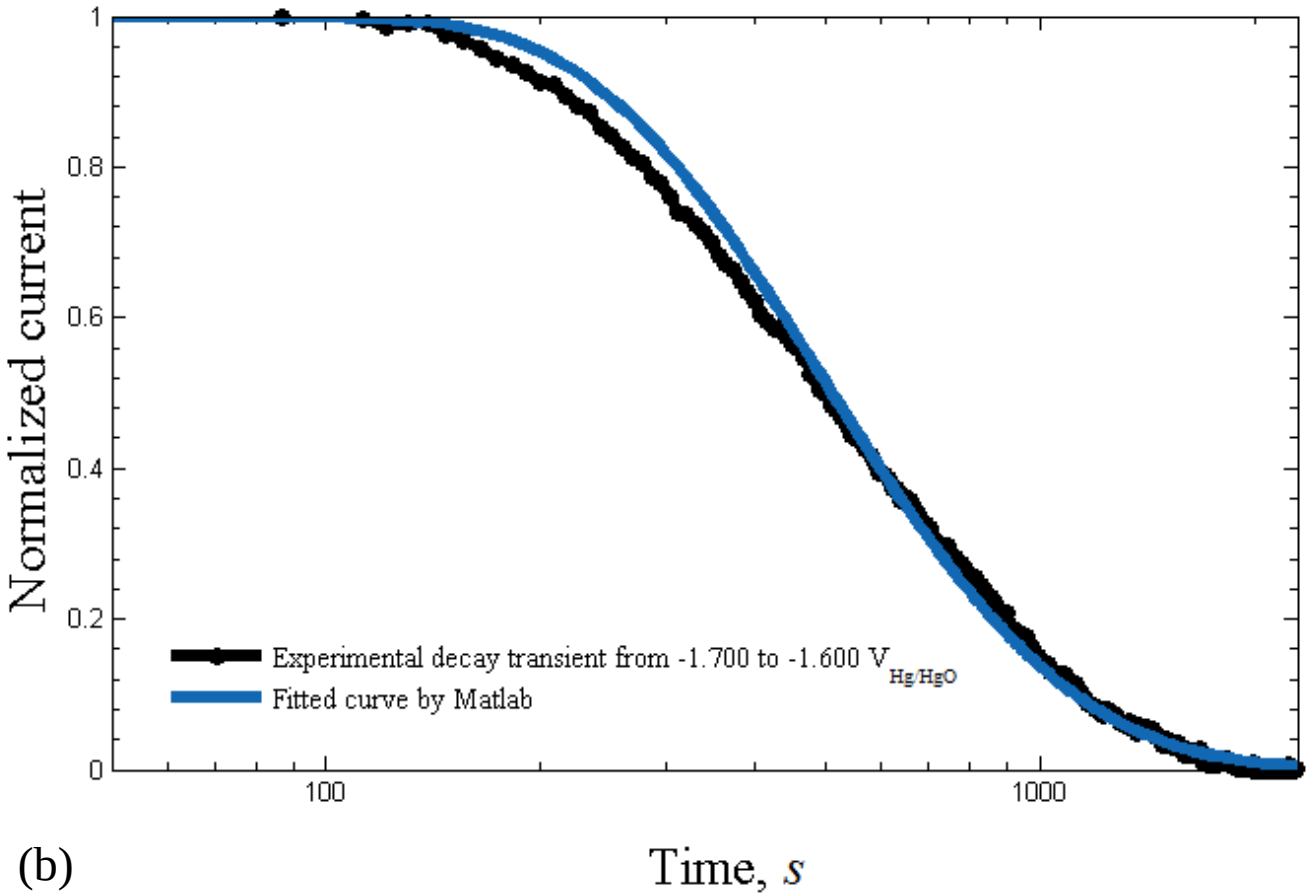

Fig. 6 Fitted curves (a) for a rise transient from -1.600 $V_{Hg/HgO}$ to -1.700 $V_{Hg/HgO}$ by Matlab and (b) for a decay transient from -1.700 $V_{Hg/HgO}$ to -1.600 $V_{Hg/HgO}$ for 980 DP-GI (650 MPa YS) specimen in 0.1 M NaOH solution. For a rise transient, the normalised current is equal to (the measured current minus the initial current) divided by (the difference between the final current and the initial current). For a decay transient, the normalised current is equal to (the initial current minus the measured current) divided by (the difference between the initial current and the final current).

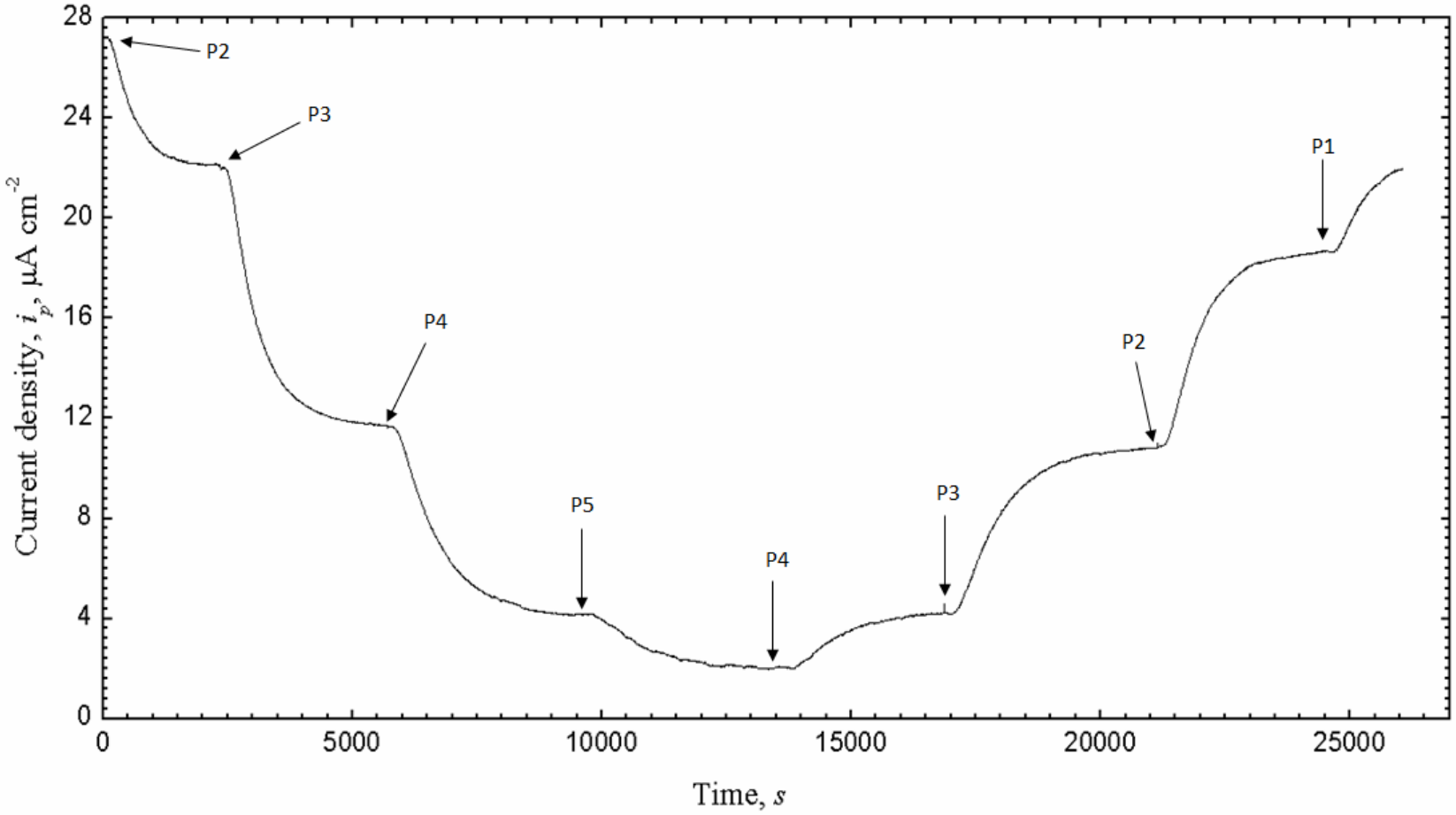

Fig. 7 Hydrogen permeation transients at different cathodic potentials at the input side of the 980 DP-GI (650 MPa YS) steel after 48 h pre-charging at – 1.600 $V_{Hg/HgO}$ in 0.1 M NaOH solution(P1: – 1.700 $V_{Hg/HgO}$, P2: – 1.600 $V_{Hg/HgO}$, P3: – 1.400 $V_{Hg/HgO}$, p4: – 1.200 $V_{Hg/HgO}$ and P5: – 1.100 $V_{Hg/HgO}$).

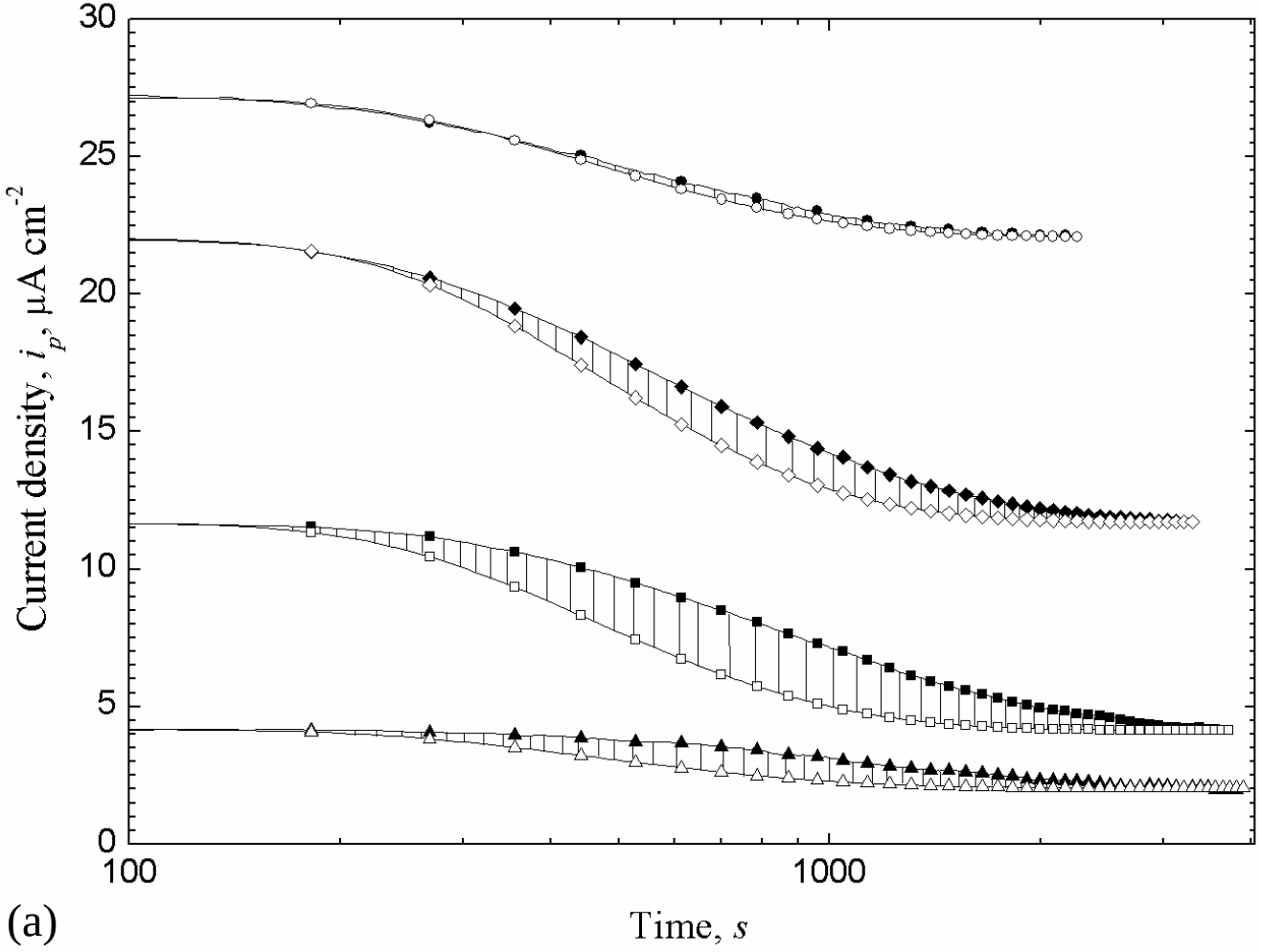

(a)

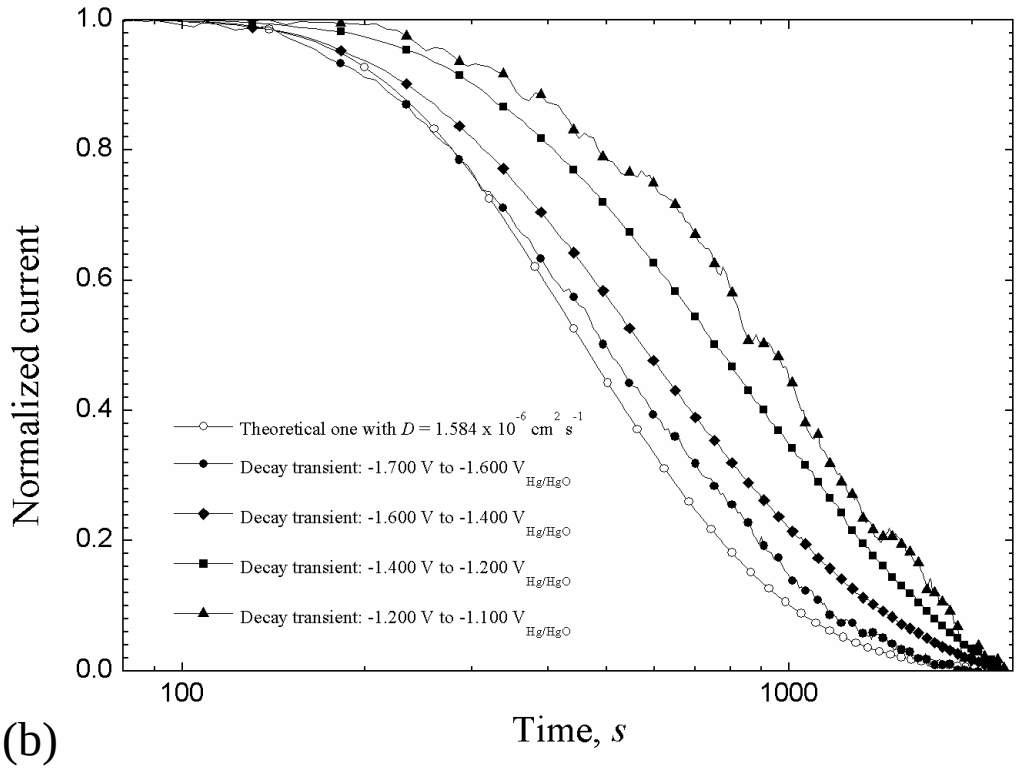

Fig. 8. (a) The area difference between the experimental permeation curves (full symbols) and the theoretical curve (open symbols) for decay transients for 980 DP-GI (650 MPa YS) in 0.1 M NaOH solution: (1) circles - experimental decay transient from -1.700 $V_{Hg/HgO}$ to -1.600 $V_{Hg/HgO}$, theoretical curve with $D = 1.584\times10^{-6}$ cm^2 s^{-1}; (2) diamonds - experimental decay transient from -1.600 $V_{Hg/HgO}$ to -1.400 $V_{Hg/HgO}$, theoretical curve with $D = 1.584\times10^{-6}$ cm^2 s^{-1}; (3) squares - experimental decay transient from -1.400 $V_{Hg/HgO}$ to -1.200 $V_{Hg/HgO}$, theoretical curve with $D = 1.584\times10^{-6}$ cm^2 s^{-1}; (4) triangles - experimental decay transient from -1.200 $V_{Hg/HgO}$ to -1.100 $V_{Hg/HgO}$, theoretical curve with $D = 1.584\times10^{-6}$ cm^2 s^{-1} and (b) the normalized experimental decay transients and the corresponded theoretical curve calculated with D value of 1.584×10^{-6} cm^2 s^{-1}. For a decay transient, the normalised current is equal to (the initial current minus the measured current) divided by (the difference between the initial current and the final current).

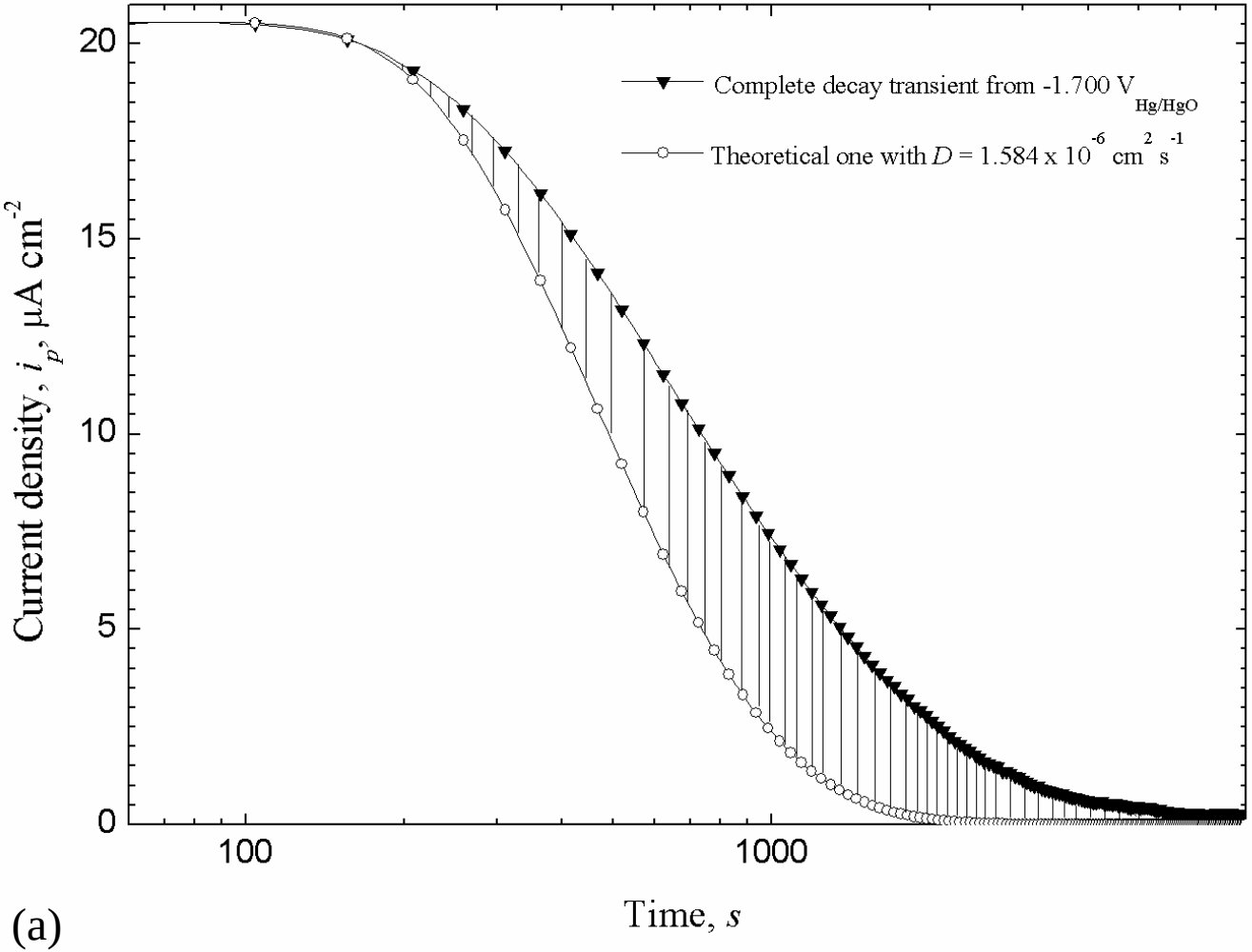
Complete decay transient from -1.700 V Hg/HgO
Theoretical one with D = 1.584 x 10^-6 cm^2 s^-1
Current density, i_p, μA cm^-2
Time, s
0
5
10
15
20
100
1000

(a)

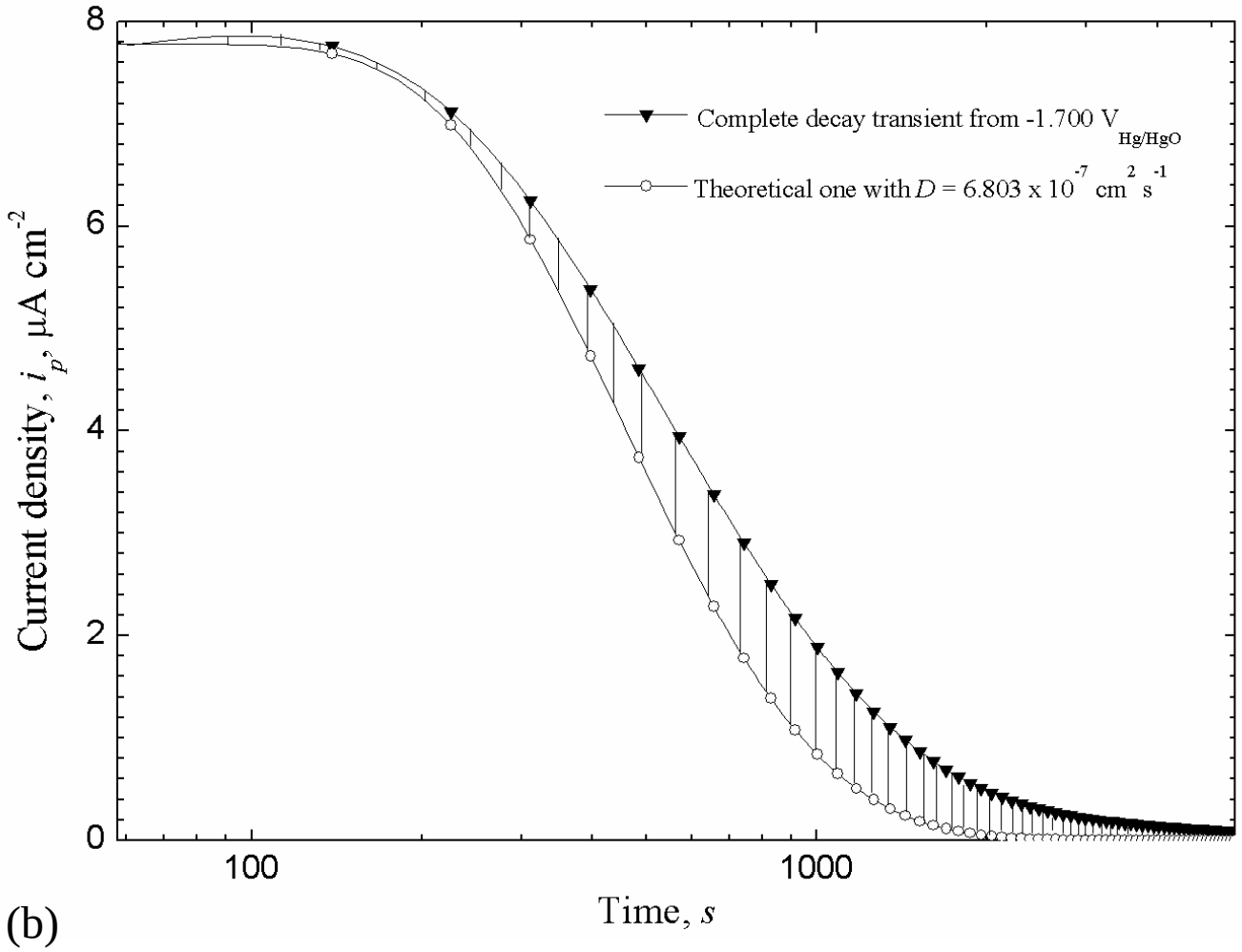

Fig. 9 The typical area difference between the experimental complete decay curve and the theoretical one for (a) 980 DP-GI (650 MPa YS) and (b) 980 QP steels, hydrogen charged in 0.1 M NaOH solution.

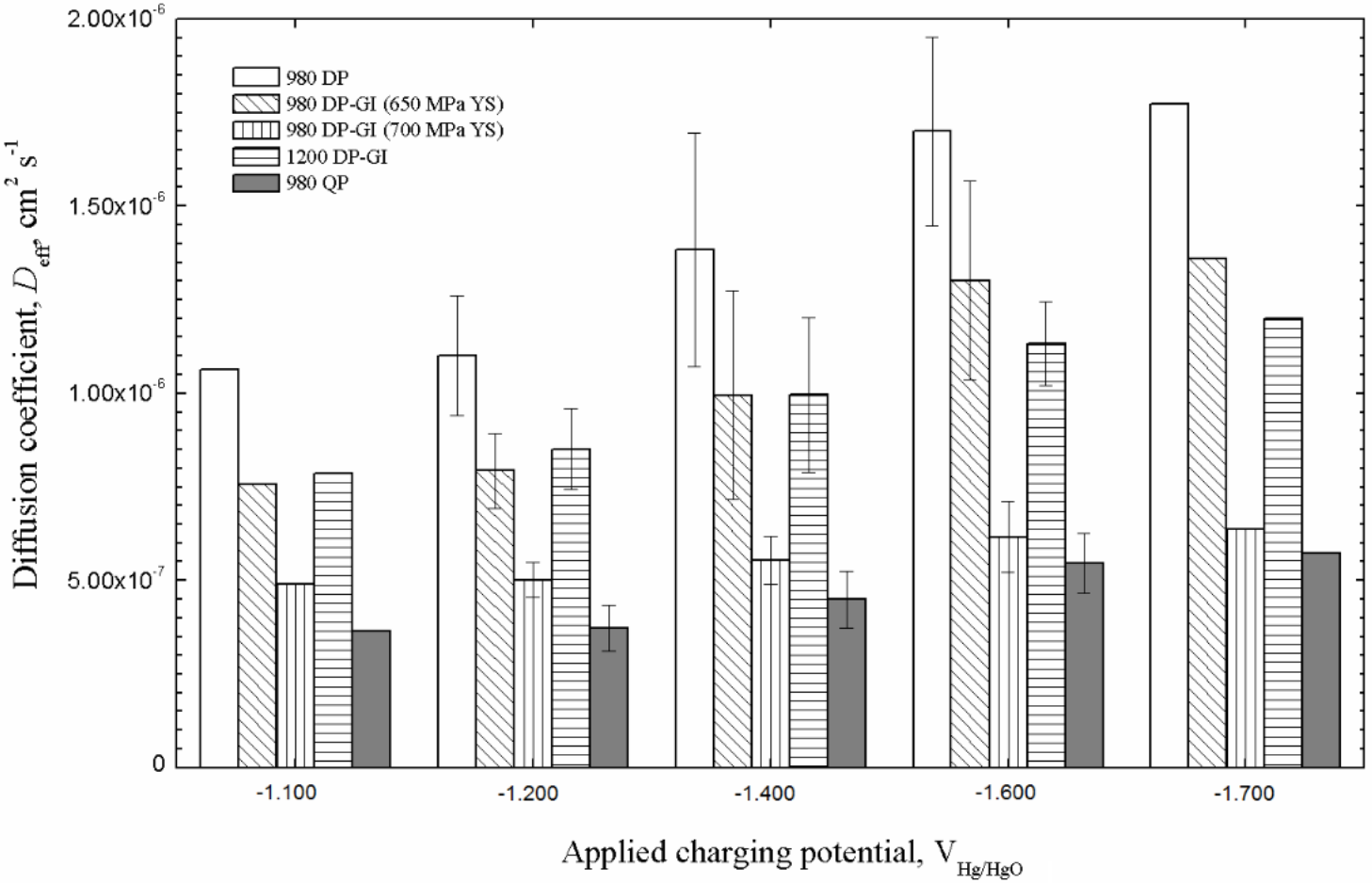

Fig. 10 Hydrogen diffusion coefficient values of the studied DP and Q&P steels during the transient loop from -1.700 $V_{Hg/HgO}$ to -1.100 $V_{Hg/HgO}$ and back to -1.700 $V_{Hg/HgO}$ in 0.1 M NaOH solution.

Table 1. Chemical composition (in wt %) and mechanical properties of the DP and QP steels.

Steel designation	C	Si	Mn	Al	Nb	Ti	Cr	Yield stress, MPa	Tensile stress, MPa	Elongation at fracture, e_f, %
980 DP	0.09	0.28	2.26	0.03	0.004	0.02	0.54	590	930	8
980 DP-GI (650MPa YS)	0.09	0.29	2.19	0.03	0.04	0.03	0.43	650	1060	8
980 DP-GI (700MPa YS)	0.08	0.41	2.18	0.03	0.04	0.05	0.02	700	1040	7
1200 DP-GI	0.12	0.24	2.43	0.03	0.02	0.03	0.56	900	1200	5
980 QP	0.20	1.39	1.88	0.04	0.03	0.006	0.03	680	1020	11

Table 2. Quantitative metallography results for the DP and QP steels.

Steel Designation	Ferrite		Martensite		Bainite		Retained austenite	
	Relative amount %	Grain size μm	Relative amount %	Grain size μm	Relative amount %	Grain size μm	Relative amount %	Grain size μm
980 DP	40%	6.8	60%	5.5	0	-	0	-
980 DP (650 MPa YS)	37%	2.1	63%	1.5	0	-	0	-
980 DP (700 MPa YS)	36%	1.1	64%	1.4	0	-	0	-
1200 DP-GI	26%	5.0	74%	4.8	0	-	0	-
980 QP	39%	9.8	0	0	53%	9.4	8%	1.3

Table 3. Permeability parameter values for the DP and QP steels obtained from experimental transients cathodically charged in 0.1 M NaOH solution.

Steel designation	Thickness (L, cm)	Working area (S, cm^2)	Starting and finishing potential for transient, ($V_{Hg/HgO}$)	i_∞ ($\mu A\ cm^{-2}$)	$i_\infty \times L$ ($\mu A\ cm^{-1}$)	D_{eff} ($cm^2\ s^{-1}$)	C_L ($mol\ m^{-3}$)	C_L ($\mu g\ g^{-1}$)
980 DP	0.053	3.394	-1.600 to -1.700	39.99	2.12	2.07×10^{-6}	10.6	1.41
			-1.600 to -1.700	39.96	2.12	2.07×10^{-6}	10.6	1.41
			-1.700 to -1.600	32.33	1.71	2.00×10^{-6}	8.55	1.14
			-1.700 to -1.600	32.02	1.70	1.88×10^{-6}	8.51	1.13
			-1.600 to -1.400	15.04	0.80	1.61×10^{-6}	4.01	0.54
			-1.400 to -1.200	4.50	0.24	1.21×10^{-6}	1.20	0.16
			-1.200 to -1.100	2.14	0.11	1.06×10^{-6}	0.55	0.07
			-1.100 to -1.200	4.32	0.23	0.99×10^{-6}	1.15	0.15
			-1.200 to -1.400	12.37	0.66	1.16×10^{-6}	3.30	0.44
			-1.400 to -1.600	24.29	1.29	1.52×10^{-6}	6.45	0.86
			-1.600 to -1.700	29.51	1.56	1.77×10^{-6}	7.81	1.04
					Average:	$1.58 \pm 0.4 \times 10^{-6}$		
980 DP-GI (650 MPa YS)	0.075	3.308	-1.600 to -1.700	27.32	2.05	1.58×10^{-6}	13.4	1.94
			-1.600 to -1.700	27.08	2.03	1.56×10^{-6}	13.3	1.92
			-1.700 to -1.600	22.34	1.68	1.55×10^{-6}	11.0	1.59
			-1.700 to -1.600	22.06	1.65	1.49×10^{-6}	10.8	1.56
			-1.600 to -1.400	11.76	0.88	1.19×10^{-6}	5.77	0.83
			-1.400 to -1.200	4.06	0.30	0.86×10^{-6}	1.97	0.28
			-1.200 to -1.100	1.96	0.15	0.76×10^{-6}	0.98	0.14
			-1.100 to -1.200	4.10	0.31	0.72×10^{-6}	2.03	0.29
			-1.200 to -1.400	10.63	0.80	0.80×10^{-6}	5.25	0.76
			-1.400 to -1.600	18.20	1.37	1.11×10^{-6}	8.99	1.30
			-1.600 to -1.700	22.07	1.66	1.36×10^{-6}	10.9	1.57
					Average:	$1.18 \pm 0.3 \times 10^{-6}$		

980 DP-GI (700 MPa YS)	0.080	3.133	-1.600 to -1.700	10.55	0.84	0.75×10^{-6}	11.5	1.46
			-1.600 to -1.700	10.21	0.82	0.76×10^{-6}	11.2	1.42
			-1.700 to -1.600	8.27	0.66	0.71×10^{-6}	9.00	1.14
			-1.700 to -1.600	7.91	0.63	0.68×10^{-6}	8.59	1.09
			-1.600 to -1.400	4.13	0.33	0.60×10^{-6}	4.50	0.57
			-1.400 to -1.200	1.94	0.16	0.54×10^{-6}	2.18	0.28
			-1.200 to -1.100	1.36	0.11	0.49×10^{-6}	1.50	0.19
			-1.100 to -1.200	1.95	0.16	0.47×10^{-6}	2.18	0.28
			-1.200 to -1.400	3.80	0.30	0.51×10^{-6}	4.09	0.52
			-1.400 to -1.600	6.34	0.51	0.55×10^{-6}	6.95	0.88
			-1.600 to -1.700	9.20	0.74	0.64×10^{-6}	10.1	1.28
					Average:	$0.61 \pm 0.1 \times 10^{-6}$		
1200 DP-GI	0.070	2.997	-1.600 to -1.700	24.74	1.73	1.26×10^{-6}	14.1	1.37
			-1.600 to -1.700	23.97	1.68	1.27×10^{-6}	13.7	1.33
			-1.700 to -1.600	20.14	1.41	1.14×10^{-6}	11.5	1.12
			-1.700 to -1.600	19.61	1.37	1.21×10^{-6}	11.2	1.09
			-1.600 to -1.400	11.59	0.81	1.14×10^{-6}	6.61	0.64
			-1.400 to -1.200	4.91	0.34	0.93×10^{-6}	2.77	0.27
			-1.200 to -1.100	2.55	0.18	0.79×10^{-6}	1.47	0.14
			-1.100 to -1.200	5.14	0.36	0.77×10^{-6}	2.94	0.29
			-1.200 to -1.400	11.95	0.84	0.85×10^{-6}	6.86	0.67
			-1.400 to -1.600	18.54	1.30	1.05×10^{-6}	10.6	1.03
			-1.600 to -1.700	21.95	1.54	1.20×10^{-6}	12.6	1.22
					Average:	$1.05 \pm 0.2 \times 10^{-6}$		
980 QP	0.048	2.930	-1.600 to -1.700	10.00	0.48	0.66×10^{-6}	7.32	1.05
			-1.600 to -1.700	9.47	0.46	0.68×10^{-6}	7.01	1.01
			-1.700 to -1.600	7.85	0.38	0.63×10^{-6}	5.79	0.83
			-1.700 to -1.600	7.38	0.35	0.61×10^{-6}	5.33	0.77
			-1.600 to -1.400	4.15	0.20	0.50×10^{-6}	3.05	0.44
			-1.400 to -1.200	1.69	0.08	0.42×10^{-6}	1.22	0.18
			-1.200 to -1.100	0.93	0.05	0.36×10^{-6}	0.76	0.11
			-1.100 to -1.200	1.74	0.08	0.33×10^{-6}	1.22	0.18
			-1.200 to -1.400	3.69	0.18	0.40×10^{-6}	2.74	0.39
			-1.400 to -1.600	5.53	0.27	0.49×10^{-6}	4.12	0.59
			-1.600 to -1.700	8.66	0.42	0.57×10^{-6}	6.40	0.92
					Average:	$0.51 \pm 0.1 \times 10^{-6}$		

Table 4. The density of reversible hydrogen trap sites in the DP and Q&P steels for the successive partial decay transients from -1.700 $V_{Hg/HgO}$ to -1.100 $V_{Hg/HgO}$. N_T was evaluated using the Oriani-Dong model. N_T^* was evaluated using the permeation curve method.

Steel designation	Starting and finishing potential for transient, ($V_{Hg/HgO}$)	η, V, (at start of transient)	i_∞, ($\mu A\ cm^{-2}$), (at end of transient)	D_{eff}, ($cm^2\ s^{-1}$), (average for transient)	N_t, (sites cm^{-3}), (at start of transient)	C_t, (mol m^{-3}), (at start of transient)	C_t, ($\mu g\ g^{-1}$), (at start of transient)	C_L, (mol m^{-3}), (at start of transient)	C_L, ($\mu g\ g^{-1}$), (at start of transient)	C_T, ($\mu g\ g^{-1}$), (at start of transient)	$C_t/(C_t + C_L)$, (%)	N_t^*, (sites cm^{-3}), (average for transient)	C_t^*, (mol m^{-3}), (average for transient)	C_t^*, ($\mu g\ g^{-1}$), (average for transient)	C_L^*, (mol m^{-3}), (at start of transient)	C_L^*, ($\mu g\ g^{-1}$), (at start of transient)	$C_t^*/(C_t^* + C_L^*)$, (%)
980 DP-GI	-1.700 to -1.600	-0.857	32.02	1.88×10^{-6}	0.65×10^{17}	0.11	0.015	10.6	1.410	1.556	1	0.69×10^{17}	0.11	0.015	11.1	1.476	1
	-1.600 to -1.400	-0.757	15.04	1.61×10^{-6}	1.82×10^{17}	0.30	0.040	8.51	1.130	1.447	3	2.91×10^{17}	0.48	0.064	8.76	1.168	5
	-1.400 to -1.200	-0.557	4.50	1.21×10^{-6}	4.42×10^{17}	0.73	0.097	4.01	0.535	0.911	15	5.15×10^{17}	0.85	0.113	5.13	0.684	14
	-1.200 to -1.100	-0.357	2.14	1.06×10^{-6}	5.93×10^{17}	0.99	0.132	1.20	0.160	0.311	45	1.31×10^{17}	0.22	0.029	1.05	0.140	17
				sum	12.8×10^{17}							10.1×10^{17}					
980 DP-GI (650 MPa YS)	-1.700 to -1.600	-0.857	22.06	1.49×10^{-6}	0.39×10^{17}	0.06	0.009	13.3	1.920	2.035	0.5	0.50×10^{17}	0.08	0.012	14.3	2.060	0.6
	-1.600 to -1.400	-0.757	11.76	1.19×10^{-6}	2.05×10^{17}	0.34	0.049	10.8	1.560	2.080	3	3.26×10^{17}	0.53	0.077	12.6	1.817	4
	-1.400 to -1.200	-0.557	4.06	0.86×10^{-6}	5.19×10^{17}	0.86	0.124	5.77	0.833	1.530	13	5.68×10^{17}	0.94	0.136	5.50	0.794	15
	-1.200 to -1.100	-0.357	1.96	0.76×10^{-6}	6.82×10^{17}	1.13	0.163	1.97	0.284	0.598	37	1.88×10^{17}	0.36	0.052	1.69	0.244	18
				sum	14.4×10^{17}							11.1×10^{17}					
980 DP-GI (700 MPa YS)	-1.700 to -1.600	-0.857	7.91	0.68×10^{-6}	0.70×10^{17}	0.12	0.015	11.2	1.420	1.572	1	0.95×10^{17}	0.16	0.020	13.1	1.658	1
	-1.600 to -1.400	-0.757	4.13	0.60×10^{-6}	1.67×10^{17}	0.28	0.036	8.59	1.090	1.383	3	1.87×10^{17}	0.31	0.039	7.27	0.922	4
	-1.400 to -1.200	-0.557	1.94	0.54×10^{-6}	2.61×10^{17}	0.43	0.055	4.50	0.571	0.804	9	2.40×10^{17}	0.40	0.051	6.25	0.793	6
	-1.200 to -1.100	-0.357	1.36	0.49×10^{-6}	3.44×10^{17}	0.57	0.072	2.18	0.276	0.415	21	1.02×10^{17}	0.17	0.022	1.60	0.203	10
				sum	8.42×10^{17}							6.24×10^{17}					
1200 DP-GI	-1.700 to -1.600	-0.857	19.61	1.21×10^{-6}	0.27×10^{17}	0.04	0.004	13.7	1.330	1.398	0.3	0.22×10^{17}	0.04	0.004	13.7	1.330	0.3
	-1.600 to -1.400	-0.757	11.59	1.14×10^{-6}	0.67×10^{17}	0.11	0.011	11.2	1.090	1.216	1	0.77×10^{17}	0.13	0.013	9.04	0.877	1
	-1.400 to -1.200	-0.557	4.91	0.93×10^{-6}	2.27×10^{17}	0.38	0.037	6.61	0.641	0.877	6	2.62×10^{17}	0.43	0.042	6.00	0.582	7
	-1.200 to -1.100	-0.357	2.55	0.79×10^{-6}	3.83×10^{17}	0.64	0.062	2.77	0.269	0.438	19	1.47×10^{17}	0.24	0.023	2.42	0.235	9
				sum	7.04×10^{17}							5.08×10^{17}					

980 QP	-1.700 to -1.600	-0.857	7.38	0.61×10^{-6}	0.81×10^{17}	0.13	0.019	7.01	1.010	1.112	2	0.71×10^{17}	0.12	0.017	12.5	1.796	1
	-1.600 to -1.400	-0.757	4.15	0.50×10^{-6}	2.21×10^{17}	0.37	0.053	5.33	0.767	1.056	7	1.01×10^{17}	0.17	0.024	7.97	1.147	2
	-1.400 to -1.200	-0.557	1.69	0.42×10^{-6}	3.97×10^{17}	0.66	0.095	3.05	0.439	0.708	18	8.51×10^{16}	0.14	0.020	3.11	0.448	5
	-1.200 to -1.100	-0.357	0.93	0.36×10^{-6}	5.40×10^{17}	0.90	0.130	1.22	0.176	0.338	42	5.51×10^{16}	0.09	0.013	1.30	0.187	7
				sum	12.4×10^{17}							3.12×10^{17}					

Table 5. The total density of reversible hydrogen trap sites in the DP and Q&P steels for the complete decay transients started at -1.700 $V_{Hg/HgO}$ evaluated using the permeation curve method. The final potential was the open circuit potential (ocp).

Steel designation	Starting and finishing potential for transient, ($V_{Hg/HgO}$)	η, V, (at start of transient)	i_∞, ($\mu A\ cm^{-2}$), (at start of transient)	D_{eff}, ($cm^2\ s^{-1}$), (average for transient)	C_T, ($\mu g\ g^{-1}$), (at start of transient)	N_t^*, (sites cm^{-3}), (average for transient)	C_t^*, (mol m^{-3}), (average for transient)	C_t^*, ($\mu g\ g^{-1}$), (average for transient)	C_L^*, (mol m^{-3}), (at start of transient)	C_L^*, ($\mu g\ g^{-1}$), (at start of transient)	Percentage of trapped hydrogen, (%),
980 DP-GI	-1.700 to ocp	-0.857	28.95	1.25×10^{-6}	1.689	18.8×10^{17}	3.12	0.416	2.65	0.353	54
980 DP-GI (650 MPa YS)	-1.700 to ocp	-0.857	20.48	0.98×10^{-6}	2.223	24.2×10^{17}	4.02	0.581	2.92	0.422	58
980 DP-GI (700 MPa YS)	-1.700 to ocp	-0.857	8.44	0.51×10^{-6}	1.737	33.0×10^{17}	5.48	0.695	3.11	0.394	64
1200 DP-GI	-1.700 to ocp	-0.857	21.61	0.88×10^{-6}	1.728	22.6×10^{17}	3.75	0.364	4.13	0.400	48
980 QP	-1.700 to ocp	-0.857	7.80	0.42×10^{-6}	1.331	5.91×10^{17}	0.98	0.141	1.90	0.273	34

Table 6. The values of reversible hydrogen trap density from the literature.

Authors	Material	Mathematic model	Assigned value to parameters	Charging conditions	Trap site density (sites cm^{-3})
Liu and Atrens [29]	3.5NiCrMoV medium strength steel	$N_t = N_L \times \left(\frac{D_L}{D_{eff}} - 1\right) \exp(-\frac{E_b}{RT})$	$D_L = 1.29 \times 10^{-6}$ cm^2 s^{-1} $N_L = 1.45 \times 10^{23}$ sites cm^{-3} $E_b = 29$ kJ mol^{-1}	Between -1.700 $V_{Ag/AgCl}$ and -1.100 $V_{Ag/AgCl}$ in 0.1 M NaOH	~ 10^{18}
Fallahmohammadi et al. [28]	X65 and F22 pipeline steel	$\frac{t_T^*}{t_L^*} - 1 = \frac{3N_t}{C_a}$	$t_L^* = L^2/6D_L$	Constant cathodic current density of 0.5 mA cm^{-2} in 0.2 mol L^{-1} CH_3COOH + 0.4 mol L^{-1} CH_3COONa	~ 10^{19}
Frappart et al. [45]	Quenched and tempered martensitic steel	$\frac{t_T}{t_L} - 1 = \frac{3N_t}{C_a}$	$t_L = L^2/15.3D_L$	Constant cathodic current density of 5-200 mA cm^{-2} in 1 M H_2SO_4	~ 10^{19}
Zhu et al. [44]	Quenching and partitioning steels	$N_t = \frac{N_A \times C_T}{3}\left(\frac{D_L}{D_{eff}} - 1\right)$	$D_L = 1.28 \times 10^{-4}$ cm^2 s^{-1} $N_A = 6.02 \times 10^{23}$ mol^{-1}	Constant cathodic current density of 7.64 mA cm^{-2} in 0.2 M NaOH + 3 g L^{-1} NH_4SCN	~ 10^{21}
Zakroczymski [27]	Armco iron	Permeation curve method	-	Complete decay from a current density of 10mA cm^{-2} in 0.1M NaOH	~ 10^{13}
Haq et al. [50]	X70 pipeline steel	$N_t = N_L \times \left(\frac{D_L}{D_{eff}} - 1\right) \exp(-\frac{E_b}{RT})$	$D_L = 7.20 \times 10^{-5}$ cm^2 s^{-1} $N_L = 7.52 \times 10^{22}$ sites cm^{-3} $E_b = 0.3$ eV	Constant cathodic current density of 3.52 mA cm^{-2} in 0.1 N NaOH + 10 g L^{-1} $Na_2S \cdot 9H_2O$	~ 10^{12}
Dong et al. [25]	X100 pipeline steel	$N_t = N_L \times \left(\frac{D_L}{D_{eff}} - 1\right) \exp(-\frac{E_b}{RT})$	$D_L = 1.28 \times 10^{-4}$ cm^2 s^{-1} $N_L = 7.52 \times 10^{22}$ sites cm^{-3} $E_b = 0.3$ eV	Constant cathodic current density of 10 mA cm^{-2} in 0.2 M H_2SO_4 + 0.25 g L^{-1} As_2O_3	~ 10^{26}
Begić Hadžipašić et al. [47]	DP and TRIP steel	$N_t = N_L \times \left(\frac{D_L}{D_{eff}} - 1\right) \exp(-\frac{E_b}{RT})$	$D_L = 1.28 \times 10^{-4}$ cm^2 s^{-1} $N_L = 7.52 \times 10^{22}$ sites cm^{-3} $E_b = 0.3$ eV	Open circuit potential (ocp) in 2 mol L^{-1} H_2SO_4	~ 10^{25}